A Combined Experimental/Analytical Approach To Support the Design of a Lightweight, Rigid-Wall, Mobile Shelter

Paul V. Cavallaro
NUWC Division Newport

Melvin Jee
U.S. Army Natick Soldier Research, Development, and Engineering Center

NAVSEA
WARFARE CENTERS
NEWPORT

Naval Undersea Warfare Center
Newport, Rhode Island

20071210001

PREFACE

Reviewed and Approved: 5 November 2007

Harriet L. Coleman

Harriet L. Coleman
Head, Ranges, Engineering, and Analysis Department

REPORT DOCUMENTATION PAGE

Public reporting for this collection of information is estimated to average 1 hour per response, including the time for reviewing instructions, searching existing data sources, gathering and maintaining the data needed, and completing and reviewing the collection of information. Send comments regarding this burden estimate or any other aspect of this collection of information, including suggestions for reducing this burden, to Washington Headquarters Services, Directorate for Information Operations and Reports, 1215 Jefferson Davis Highway, Suite 1204, Arlington, VA 22202-4302, and to the Office of Management and Budget, Paperwork Reduction Project (0704-0188), Washington, DC 20503.

1. AGENCY USE ONLY (Leave blank)	2. REPORT DATE 5 November 2007	3. REPORT TYPE AND DATES COVERED

4. TITLE AND SUBTITLE

A Combined Experimental/Analytical Approach To Support the Design of a Lightweight, Rigid-Wall, Mobile Shelter

5. FUNDING NUMBERS

6. AUTHOR(S)

Paul V. Cavallaro
Melvin Jee

7. PERFORMING ORGANIZATION NAME(S) AND ADDRESS(ES)

Naval Undersea Warfare Center
1176 Howell Street
Newport, RI 02841-1708

8. PERFORMING ORGANIZATION REPORT NUMBER

TR 11,837

9. SPONSORING/MONITORING AGENCY NAME(S) AND ADDRESS(ES)

10. SPONSORING/MONITORING AGENCY REPORT NUMBER

11. SUPPLEMENTARY NOTES

12a. DISTRIBUTION/AVAILABILITY STATEMENT

Approved for public release; distribution is unlimited.

12b. DISTRIBUTION CODE

13. ABSTRACT (Maximum 200 words)

Sandwich panel construction (SPC), which is widely utilized in aircraft design, is particularly advantageous for meeting the stringent structural and weight requirements of lightweight, mobile, military systems. Mobile, rigid-wall shelters must be certified for several transport loading environments, including rail impact (vehicle mounted and dismounted), drop shock, mobility, and external air transport. This technical report documents an investigation into the survivability of an SPC mobile, rigid-wall shelter after it has been exposed to a conventional air blast event. This study used a combined experimental/analytical approach at the material and substructural levels to (1) generate accurate shelter models, (2) validate the material and substructural models, and (3) maximize the shelter's global performance against a conventional air blast event early in the design stage to avoid costly physical tests.

14. SUBJECT TERMS

Sandwich Panel Construction   Mobile Military Shelters
Material-Level Testing   Substructural-Level Tests Finite Element Analysis

15. NUMBER OF PAGES
76

16. PRICE CODE

17. SECURITY CLASSIFICATION OF REPORT Unclassified	18. SECURITY CLASSIFICATION OF THIS PAGE Unclassified	19. SECURITY CLASSIFICATION OF ABSTRACT Unclassified	20. LIMITATION OF ABSTRACT SAR

NSN 7540-01-280-5500

Standard Form 298 (Rev. 2-89)
Prescribed by ANSI Std. Z39-18
298-102

TABLE OF CONTENTS

LIST OF ILLUSTRATIONS

LIST OF ILLUSTRATIONS (Cont'd)

LIST OF TABLES

LIST OF ABBREVIATIONS AND ACRONYMS

3-D	Three-dimensional
DOF	Degree of freedom
EAT	External air transport
EBT	Euler beam theory
FEA	Finite element analysis
HMMWV	High-mobility, multipurpose wheeled vehicle
HPC	Homogeneous panel construction
LVDT	Linear variable displacement transducer
SPC	Sandwich panel construction
SRSS	Square root sum of squares

A COMBINED EXPERIMENTAL/ANALYTICAL APPROACH TO SUPPORT THE DESIGN OF A LIGHTWEIGHT, RIGID-WALL, MOBILE SHELTER

INTRODUCTION

Lightweight, rigid-wall shelters used in mobile military operations are often constructed of sandwich panels consisting of thin face sheets and thick, yet ultralight, core materials to minimize weight while maximizing structural integrity. The key structural advantage of sandwich panel construction (SPC) versus homogeneous panel construction (HPC) is the potential for up to an order of magnitude weight reduction while matching equivalent bending stiffnesses. Additional advantages include increases in damping, acoustic and thermal insulation, and possibly ballistic protection performance for a given areal weight density. These advantages, however, come at a cost, which often impacts the design and manufacturing complexities of critical joints used to connect the sandwich panels in a box-like assembly. Furthermore, stiffnesses of these joints are often difficult to characterize, and their finite values significantly influence panel deflections and rotations.

Mobile, rigid-wall shelters must be certified for several transport loading environments, including rail impact (vehicle mounted and dismounted), drop shock, mobility and external air transport. This effort addresses the ability of mobile, rigid-wall shelters to survive the effects of a conventional air blast. The study employed combined experimental and analytical approaches at the material and substructural levels to (1) generate accurate shelter models, (2) validate the material-level and substructural-level models, and (3) maximize the shelter's global performance against a conventional air blast event early in the design stage to avoid costly physical tests.

The material-level tests focused on the mechanics of the assembled constituents that formed the sandwich panel and the benchmarking of an appropriate finite element to predict the displacement, stress, and strain responses. The substructural-level tests focused on loading a structurally representative shelter section to determine the joint behaviors and stiffnesses for model benchmarking purposes.

Finally, a complete mobile, rigid-wall, military shelter model was constructed, and its modal behavior was characterized followed by its complete dynamic response to an air blast event.

1

APPROACH

A lightweight, rigid-wall shelter was constructed for mounting on various military vehicles, such as the high-mobility, multipurpose wheeled vehicle (HMMWV) shown in figure 1. The shelter was primarily constructed of thin aluminum alloy face sheets (skins) that were adhesively bonded to a relatively thick paper honeycomb core. This construction formed an SPC system that was interconnected with various aluminum extrusions, weldments, mechanical fasteners, and adhesive bonds. The structural and lightweight advantages result from the decoupling of bending and shear behaviors between face sheet and core materials; that is, the bending stiffness is materially dependent on the face sheets, and the shear stiffness is materially dependent on the core. No appreciable bending strain energies develop in the core, and no appreciable transverse shear strain energies develop in the face sheets. The decoupling of these behaviors enables the designer to achieve a level of tailorability that is unmatched by homogeneous materials but analogous to fiber-reinforced laminates.

Figure 1. Lightweight, Rigid-Wall Shelter Mounted on a HMMWV

The face sheets were 0.025-inch-thick aluminum 6061-T6 alloy except in the wheel well region, where the face sheets were 0.015-inch-thick aluminum 2024-T4 alloy. Strength properties[1] for these alloys are shown in table 1.

Table 1. Strength Properties of Aluminum Face Sheets

Aluminum Alloys	Yield Stress (psi)	Ultimate Stress (psi)
2024-T4	45,000	68,000
6061-T6	40,000	47,000

Two grades of Hexcel® WR-II Kraft®-coated paper honeycomb core were used.[2] Non-floor sandwich panels used WR-II-3/8-2.5 honeycomb core. This grade has a 3/8-inch cell size and a 2.5-lb/ft³ weight density. The floor sandwich panel used WR-II-3/8-3.8 honeycomb core, which has a 3/8-inch cell size but a higher weight density of 3.8 lb/ft³. This denser grade was required to prevent crushing deformations of the floor caused by internal equipment and soldier payloads. Compression and transverse shear properties for both grades are shown in table 2. Note that the shear strengths, which decreased with increasing thickness, represent 83% of the published strengths because of the required adjustments for thickness correction in accordance with manufacturer guidelines.

Table 2. Compression and Transverse Shear Properties for 1.210-Inch-Thick WR II Honeycomb

WR II Honeycomb Core	Compression Properties (psi)			Transverse Shear Properties (psi)			
	Bare	Stabilized		Across Ribbon Direction		Along Ribbon Direction	
	Strength	Strength	Modulus	Strength	Modulus	Strength	Modulus
3/8 cell, 2.5lb/ft³	260	340	33,000	141	13,000	83	7,000
3/8 cell, 4.0lb/ft³	515	570	55,000	212	19,000	145	9,000

The shelter generally comprises two primary sandwich panels. Each of these panels was folded into three planar sections: one panel formed the floor, front-end wall, and roof, and the second panel formed the road-side wall, door-end wall, and curb-side wall. Living hinges were formed by localized creasing along the fold lines using a specially designed fixture. This hinge method enabled the panels to be easily aligned to net shape for subsequent joining using mechanical fasteners, closeout extrusions, and weldments to form the desired closed-box configuration. The sandwich panel edges were fitted with various aluminum closeout extrusions that were adhesively bonded and mechanically fastened between the face sheets and along their edges. The connections between panels were made by way of mechanical joints comprising the closeout extrusions, corner caps, fasteners, and various weldments.

The purpose of the two primary sandwich panels was to reduce the number of joints and facilitate the manufacturing process. The rear wall included a door and related extrusions for structural reinforcement. The shelter had a forward-wall stiffener, three blast-hoop stiffeners, and a variety of extrusions to facilitate integration of electronic equipment. Experience has demonstrated that, for similar SPC rigid-wall shelters subjected to side-on air blasts, structural failures initiated along the side wall/wheel well interface from excessive flexure stresses; therefore, three hoops of continuous stiffeners internal to the sandwich panels were designed for increasing both the strength and stiffness of the shelter. These stiffeners were designed to provide the additional blast resistance while providing (1) no impact on the interior shelter volume, (2) no interference with rack-mounted equipment, and (3) a minimal weight increase.

A critical step in the efficient development of the shelter was the integration of experimental validation tests with an analytical design approach. Because of the structural complexity and unanticipated characteristics in structural behavior that analysis could not predict without prior empirical knowledge, a design approach based solely on analysis would lack the necessary robustness to accurately predict both global (panels) and local (joints) structural behavior. Conversely, a fully experimental or "make and break" approach would require fabrication and testing of multiple prototypes in an iterative process that would (1) generate excessive development costs, (2) result in long lead times, and (3) be only marginally successful from an optimization perspective. In the absence of experimentally measured performance data, the validity of analytical results could not be confirmed for this structure; therefore, a test plan was developed and subsequently justified to identify and characterize load-sharing mechanisms, panel shear and flexure stiffnesses, deflections, and stress states at both the material and structural levels.

The material level tests focused on the mechanics of the assembled constituents that form the sandwich panel in a simple beam-like geometry and the selection of an appropriate finite element that accurately predicted the displacement, stress, and strain responses of each sandwich panel component. These tests further identified potential panel failure modes that could result from flexure loading of the full structure.

The substructural level tests focused on loading a section of the shelter that was structurally representative of the full shelter in terms of construction (closeout extrusions, weldments, mechanically fastened joints, adhesive bonds, etc.), restraints, and dominant mode of loading (flexure). The goal of these tests was not to experimentally validate the shelter for any specific loading event, but rather to obtain strain and deflection data for model benchmarking. Once the model was sufficiently developed and accurately correlated with experimental results, the analysis methods could then be applied with confidence to the full structure and the specific shelter load cases to be considered.

MATERIAL-LEVEL TESTING

The material level tests focused on the mechanics of an adhesively bonded aluminum/honeycomb sandwich panel subjected to flexure loads (that is, the dominant loading mode for blast overpressure events). Four-point flexure tests were performed on six 20-inch-long by 4-inch-wide by 1.26-inch-thick sandwich beams as shown in figure 2. Four-point loading (rather than three-point loading) was selected to mitigate failures by localized core crushing prior to the onset of face sheet yielding and to provide a gage section region subjected to constant bending stress with no transverse shear stresses.
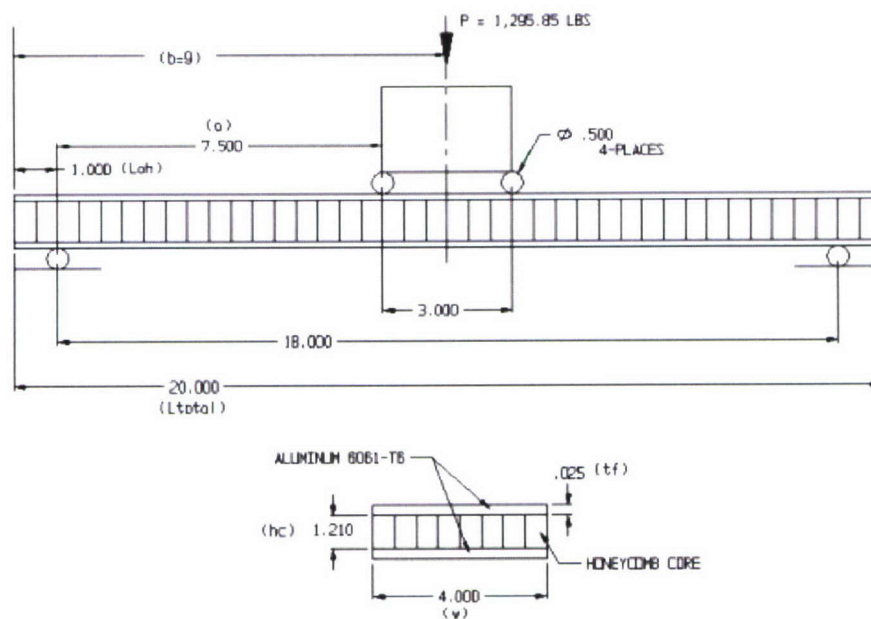
Figure 2. Four-Point Flexure Test Specimen

The honeycomb ribbon direction was oriented along the longitudinal axis of the beams. Uniaxial strain gages were adhered to the centers of both face sheets. The center location was chosen to avoid localized effects in the vicinity of the load points but keeping within the region of constant maximum moment. Although the appearance of the sandwich construction was basic, it represented a relatively complex assemblage of structural materials in which a variety of failure modes were possible. These modes included: (1) core crushing, (2) core crimping (shear), (3) face sheet/core delamination, (4) intra-cell buckling (dimpling), and (5) face sheet fracture. The observed failure mode for each of the 10 panels tested was transverse shearing of the honeycomb core. Failures occurred at both the load points and support points. The midspan deflections, peak face sheet strains, and applied loads are summarized in table 3.

Table 3. Results of Material Level Four-Point Flexure Tests

Spec. #	Total Load (lbs)	Maximum Moment (in-lbs)	Maximum Shear Force (lbs)	Tensile Face Sheet Strain (in/in)	Compressive Face Sheet Strain (in/in)	Maximum Face Sheet Axial Stress (psi)	Maximum Honeycomb Transverse Shear Stress (psi)	Mid-Span Deflection (in)
1	1,021.06	3,828.98	510.53	3,176.75	-3,135.88	31,627.11	103.33	0.251
2	1,038.57	3,894.64	519.29	3,094.18	-3,049.98	32,169.48	105.10	0.250
3	955.37	3,582.64	477.69	2,880.68	-2,713.87	29,592.37	96.68	0.252
4	857.66	3,216.23	428.83	2,509.54	-2,434.48	26,565.83	86.80	0.194
5	971.14	3,641.78	485.57	2,874.00	-2,876.51	30,080.85	98.28	0.220
6	1,052.46	3,946.73	526.23	3,236.80	-3,062.49	32,599.72	106.51	0.237

Correlation of the finite element analysis (FEA) results to the four-point bend test data validated the ability of the sandwich element model to accurately predict the (1) distribution of bending stresses within the face sheets, (2) transverse shear stresses in the honeycomb core, (3) interlaminar shear stresses within the adhesive layers, (4) bending and transverse shearing components of the total deflection, (5) load required to fail the honeycomb core in shear, (6) load required to fail the adhesive layer between the honeycomb core and face sheets, and (7) load required to initiate yielding of the face sheets.

The design of an SPC for structural applications is analogous to that of I-beams, where the face sheets (flanges) are designed to support flexure loads while the core (web) supports the transverse shear loads.[3] An extension of Allen's[4] analysis for SPC consisting of relatively thin, yet stiff, face sheets and relatively thick, but compliant, core layer was performed to investigate the effects of the honeycomb core's transverse shear modulus on the deflection response of the four-point bend specimens.

Assuming linear elasticity and symmetric face sheets, the small deflection theory was invoked, whereby the midplane was assumed to be coincident with the neutral surface. The neutral surface by definition is a surface having no bending stresses or deformations due to bending. In-plane axial stresses acting on the neutral surface are referred to as "membrane stresses." SPCs by design have considerable bending stiffness. If membrane stresses exist, the coupled effects between bending and membrane stresses (analogous to load stiffening of beams) must be considered—resulting in the need for a large deflection (nonlinear) solution. The need for large deflection solutions of homogeneous plates may be necessary even for the case of transverse loads alone; however, for SPCs conforming to the following restrictions, the small

deflection theory should be sufficient: (1) the SPC is constructed with a relatively thick, compliant core layer (that is, negligible elastic moduli but appreciable transverse shear moduli); (2) the face sheets are symmetric in both material properties and thickness; (3) the SPC is subjected to only transverse loads; and (4) no membrane stresses exist on the neutral surface.

The following analysis invokes linear elasticity (small deformation theory) and describes the midspan deflection δ, face sheet longitudinal stress σ_{xx}, face sheet longitudinal strain ε_{xx}, and core transverse shear stress τ_{xz} as functions of applied load. From Euler Beam Theory[5] (EBT), the face sheet longitudinal stress σ_{xx} from flexure loading is a linear function of the bending moment M, distance y from neutral surface to point of interest, and area moment of inertia I, resulting in a sandwich beam having a total thickness of

$$\sigma_{xx} = \frac{My}{I},$$ (1)

where $\dfrac{-t_{total}}{2} \leq y \leq \dfrac{+t_{total}}{2}$.

The maximum face sheet longitudinal stress σ_{max} is obtained at locations of maximum moment and distance farthest from the neutral axis. For the case of four-point flexure loading of symmetric sandwich beams, σ_{max} becomes

$$\sigma_{max} = \frac{\left(P_{max}\dfrac{a}{2}\right)\left(\dfrac{t_c + 2t_f}{2}\right)}{\dfrac{w}{12}\left(t_c + 2t_f\right)^3},$$ (2)

where t_c is core thickness, t_f is face sheet thickness, w is the width of the cross section, a is the distance between load and support point, and P_{max} is the maximum applied machine load.

For an isotropic material, the face sheet longitudinal strain ε_{max} corresponding to σ_{max} is obtained by assuming a uniaxial stress field:

$$\varepsilon_{max} = \frac{\sigma_{max}}{E_{xx}},$$ (3)

where E_{xx} is young's modulus in the x-direction.

Castigliano's second theorem was used to derive an expression for maximum lateral deflection based on considering the combined strain energies due to bending of the face sheets and transverse shearing of the honeycomb core. This expression is equivalent to a Timoshenko beam solution in which the effect of transverse shear deformation on lateral deflection is included.[6] The maximum deflection δ_{total} is the sum of the midspan contributions from the face sheet bending deformations and the core transverse shearing deformation:

$$\delta_{total} = \frac{Pa(3b^2 - a^2)}{E_f w\left[(t_c + 2t_f)^3 - t_c^3\right]} + \frac{3Pa}{5G_c wt_c}, \tag{4}$$

where b is the distance between load points and G_c is the core transverse shear modulus.

The total flexural rigidity D_s of the sandwich is computed using the parallel axis theorem and young's modulus for each layer as

$$D_s = \frac{E_f wt_f^3}{6} + \frac{E_f wt_f}{2}d^2 + \frac{E_c w}{12}t_c^3, \tag{5}$$

where d is the distance between face sheet midplanes.

Transverse shear stress τ_{xzc} in the core as a function of the through-thickness variable y_c is then given as

$$\tau_{xzc}(y_c) = \frac{V}{2D_s}\left[E_f t_f d + E_c\left(\frac{t_c^2}{4} - y_c^2\right)\right], \tag{6}$$

where V is the shearing force,

$$\frac{-t_c}{2} v_c \le \frac{+t_c}{2}.$$

If $E_c \ll E_f$, then the transverse shear stress of the honeycomb core is constant through the thickness as the product involving E_c becomes negligible. The transverse shear stress distribution in either face sheet (both face sheets assumed to be of equal thickness and material) as a function of the through-thickness variable y_f is

$$\tau_{xzf}(y_f) = \frac{V}{D_s}\left[\frac{(t_c^2 + 4t_c t_f + t_f^2 - 4y_f^2)E_f}{8}\right], \tag{7}$$

where $0 \le y_f \le t_f$. The maximum value of τ_{xyf} occurs at the inner surface of the face sheet.

To determine the applied load required to initiate yielding of the face sheets, the yield stress of aluminum 6061-T6 ($\sigma_{yield} = 40{,}000$ psi) was substituted into equation (1) and P_{max}, where $P_{yield} = P_{max}$, was solved for, yielding

$$P_{yield} = 1295.85 \text{ lb.}$$

The corresponding deflection terms, axial face sheet strain ($E_f = 10 \times 10^6$ psi) and honeycomb transverse shear stress (for WR-II-3/8-2.5 honeycomb along the ribbon direction, $G_c = 13{,}000$ psi and $\tau_{xzc\_allowable} = 141$ psi (thickness correction factor included on transverse shear strength)) at yield are

$$\delta_{shear} = \quad 0.093 \text{ inch,}$$
$$\delta_{bend} = \quad 0.198 \text{ inch,}$$
$$\delta_{total} = \quad 0.291 \text{ inch,}$$
$$\varepsilon_{yield} = \quad 0.004 \text{ inch/inch, and}$$
$$\tau_{xzc} = 131.0 \text{ psi.}$$

The transverse shearing deformation contributed 32% toward the total midspan deflection. Because the sandwich is symmetric and linear elasticity (small deformation) is assumed, the above strain represents the magnitude of strain in both the tensile (lower) and compressive (upper) face sheets. The continuity of τ_{xz} across the face sheet/core interface is checked by solving equation (7) at $y_f = 0$ and comparing that value to the value of τ_{xyc}. Then,

$$\tau_{xzf} = 131 \text{ psi.}$$

The effect of core transverse shear stiffness G_c on the midpoint deflection is shown in figure 3 for the above loading, material properties, and specimen dimensions. Note that δ_{bend} equals the difference between the two curves shown.
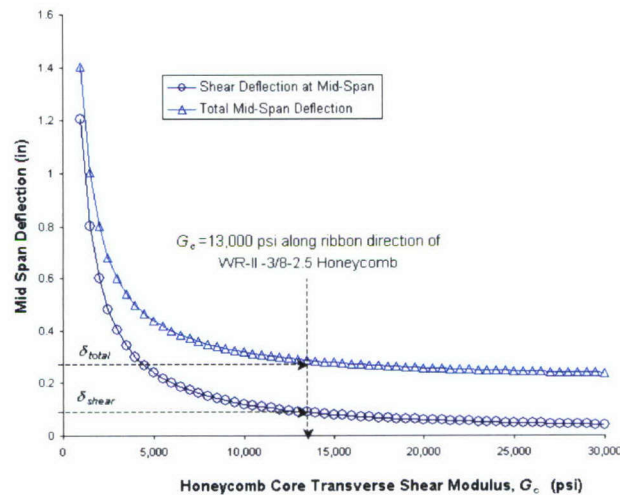
Figure 3. Effect of Honeycomb Core Transverse Shear Modulus G_C on Midspan Deflections

The NISA[7] finite element program was used to model the four-point bend test specimen. Two models were generated using the sandwich element (type-33) and the solid composite element (type-7). The sandwich element was an eight-noded laminated shell element that supported membrane-bending coupling and transverse shear deformations. Each node had six degrees of freedom (DOFs) consisting of three translations ($u1$, $u2$, and $u3$) and three rotations ($\alpha1$, $\alpha2$, and $\alpha3$); however, the rotational DOF normal to the element surface $\alpha3$, commonly referred to as the "drilling DOF," possessed no rotational stiffness. This element was developed for thick shells consisting of two or more face sheets and one or more cores. Figure 4 shows the stress components for a general three-dimensional (3-D) laminated composite. The face sheets were restricted to states of plane stress (σ_{xx}, σ_{yy}, and σ_{xy}), and the core supported only transverse

8

shear stresses (σ_{xz} and σ_{yz}). At the interface between the face sheets and the honeycomb core, the interlaminar shear stresses σ_{zx} and σ_{zy} were of particular interest. Here, these stresses represented the in-plane shear stresses within the adhesive layer and, when compared to the allowable shear strength of the adhesive, can be used to predict adhesive shear failures. The solid composite element was a laminated brick element formulated by using general 3-D states of stress (σ_{xx}, σ_{yy}, σ_{zz}, σ_{xy}, σ_{xz}, and σ_{yz}) with each node having three translational DOFs only. The layers of both the sandwich element and the composite solid element were assumed perfectly bonded together. Although the sandwich element did not support through-thickness deformations, which were expected to be negligible for global shelter models, it was considered to be significantly more efficient (computationally) than the solid composite element. Use of the solid composite element for a full shelter model would not be practical because of the level of mesh refinement required. The solid composite element, however, was preferred in localized models where 3-D stress states and through-thickness deformations were prevalent in joints, weldments, adhesive bonds, and fastener regions.
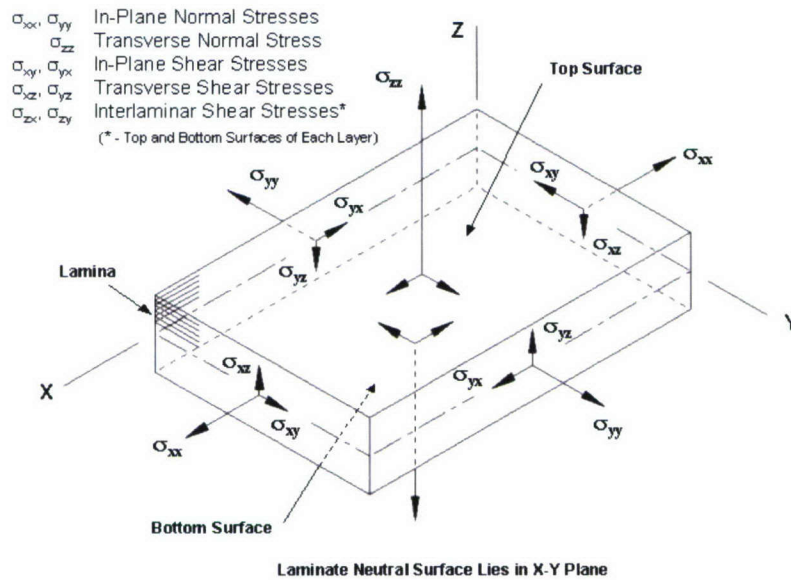
Figure 4. General 3-D Stress Components for Laminated Composites

Displacement and stress results of the sandwich element model subjected to a total load of 1295.85 lb are shown in the contour plots in figures 5 through 7. At maximum load, the peak total displacement of 0.278 inch occurred at the midspan and varied by only 4.5% of the analytical solution provided by equation (4). The magnitudes of the maximum axial stress σ_{xx} in the tensile and compressive face sheets were equal to 40,400 psi, which varied by only 1.0% of equation (2). The maximum transverse shear stress σ_{xz} in the honeycomb core (figure 7), remote from localized effects of the load points, was 138.0 psi, which varied by 5.4% of the predicted value from equation (6).
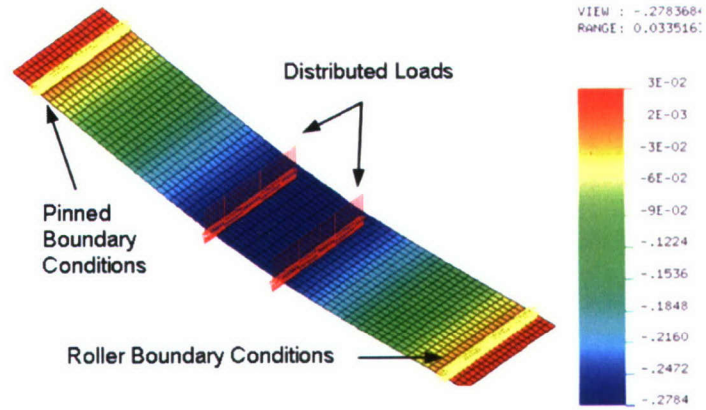
Figure 5. Transverse Displacement Contour Plot
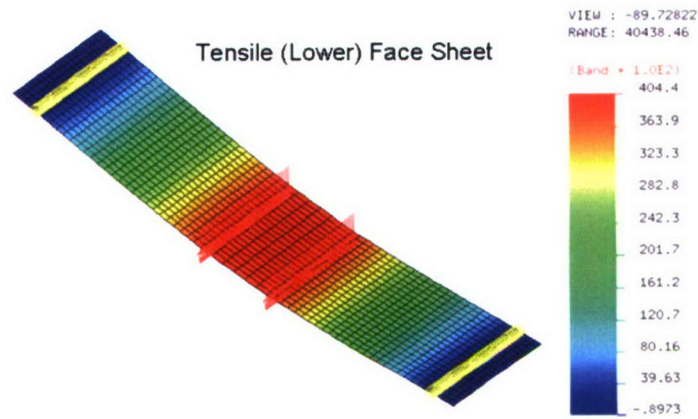
Figure 6. Axial Stress σ_{xx} Contour Plot for the Tensile (Lower) Face Sheet
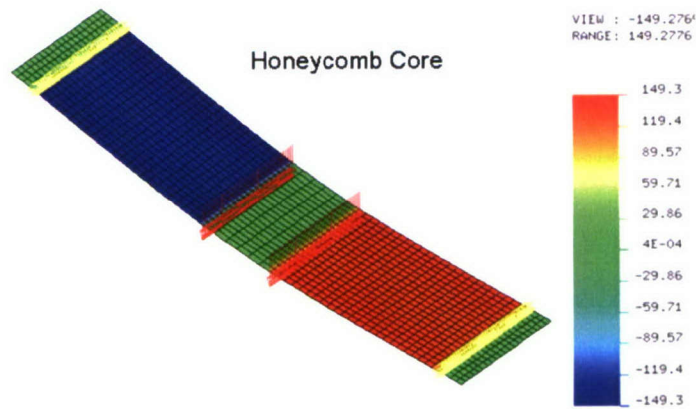
Figure 7. Transverse Shear Stress σ_{xz} Contour Plot for the Honeycomb Core

The solid composite element model shown in figure 8 captured the linear elastic through-thickness deformations at the load and support points. For the same maximum load used in the sandwich model and closed-form solution, the maximum displacement of the composite solid element model was 0.282 inch at the midspan. This model, however, did not include the effects of plasticity (stress softening) due to localized yielding of the compressive face sheet, which was evident in the tests. Post-test inspections revealed that the permanent indentations made at either the load or support points ranged in depth up to 0.06 inch. The maximum axial stresses σ_{xx} in the tensile and compressive face sheets were 40,290 psi and –40,080 psi, respectively. The maximum transverse shear stress σ_{xz} in the honeycomb core was 141.1 psi.
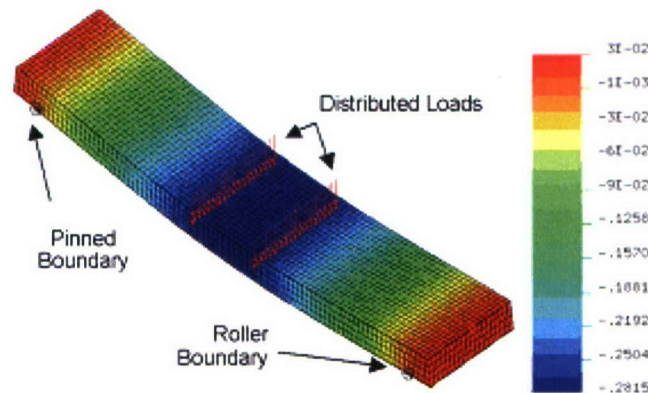
Figure 8. Contour Plot of Vertical Displacement in Inches from Composite Solid Element Model at 1295.85-lb Total Load

A comparison of the midspan deflections from the closed-form solution, finite element models, and experimental tests is shown in figure 9. The maximum load used in both the closed form and finite element solutions was used to normalize the experimental deflections. The experimental deflections were expected to slightly exceed those predicted by the closed-form and finite-element methods because localized indentations observed in the tests and solid composite element model at the load and support points could not be simulated in the closed-form solution and sandwich element model. The closed-form and FEA solutions were based on linear elasticity and did not include any geometric or material nonlinearities due to large deformations, plasticity, etc.

The material level flexure tests and subsequent modeling verified the significance of incorporating a shear deformable analysis method for developing the shelter. Both the sandwich and solid composite elements were successfully benchmarked for use in developing models of the full shelter provided that the limitations of linear elasticity were not exceeded.

11
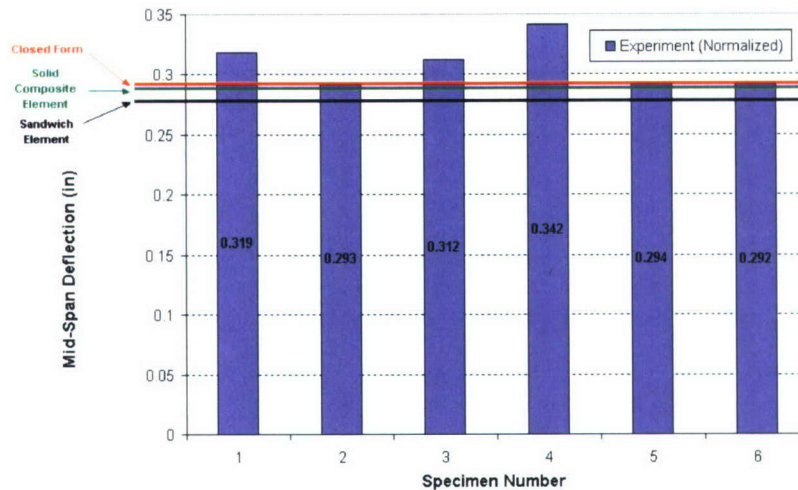
Figure 9. Comparison of Midspan Deflections for Normalized 1295.85 lb-Applied Load

REPRESENTATIVE STRUCTURAL TESTING AND DETERMINATION OF JOINT ROTATIONAL STIFFNESSES

The test specimen configuration shown in figures 10 and 11, along with its restraints and four-point loading arrangement, was specifically designed to generate high flexure stresses along the shelter's hoop direction because flexure was the dominant mode resulting from blast overpressure loads. The test configuration represented nearly one lateral half of the shelter without the forward and rear walls. The honeycomb core was oriented so that the ribbon direction was parallel to the shelter hoop axis. As with the beam flexure tests, four-point, rather than three-point, loading was selected to mitigate failures by localized core crushing prior to yielding of the face sheets. Two clamped point restraints, located at each end of the floor "D"-extrusion (fore and aft of the wheel well), were necessary for generating substantial flexure stresses at the side wall/wheel well interface.

Absent these clamped restraints, analysis demonstrated that (1) flexure stresses within the side-wall/wheel-well region were minimal and (2) the floor panel would fail by excessive bending deflections, which were not admissible during a blast event. In a realistic blast event of the full shelter, the shelter floor would bottom out against the vehicle's cargo area floor. The edges of the floor and roof panels were bolted to the test frame with clamping plates to provide nearly rigid boundary conditions.
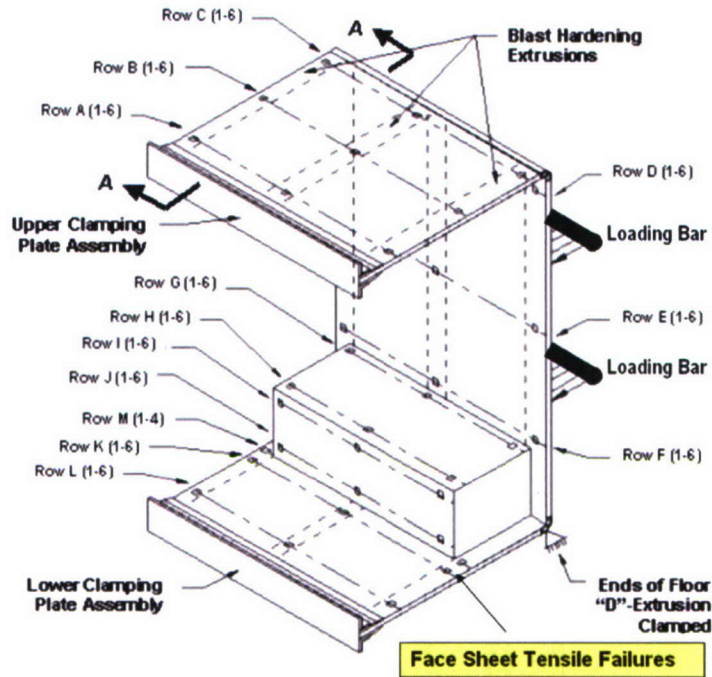
12

Figure 10. Shelter Section Test and Strain Gage Map
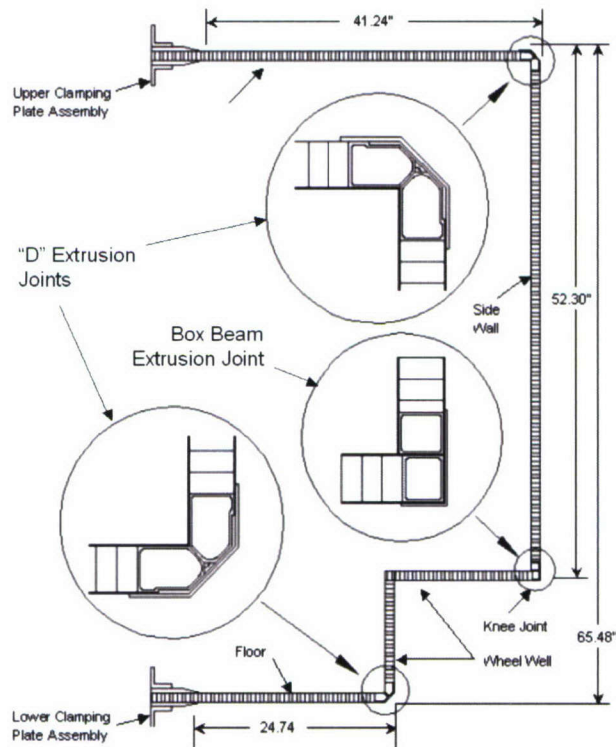
Figure 11. Cross-Sectional View of Representative Shelter Test Section

13

The joints of particular focus in the structural test specimens are the roof-to-side-wall joints and the floor-to-side-wall joints—all of which are constructed with aluminum D-extrusions designed with faceted surfaces to facilitate the construction of 90° corner connections. See figure 12 for an exploded view of a D-extrusion joint.
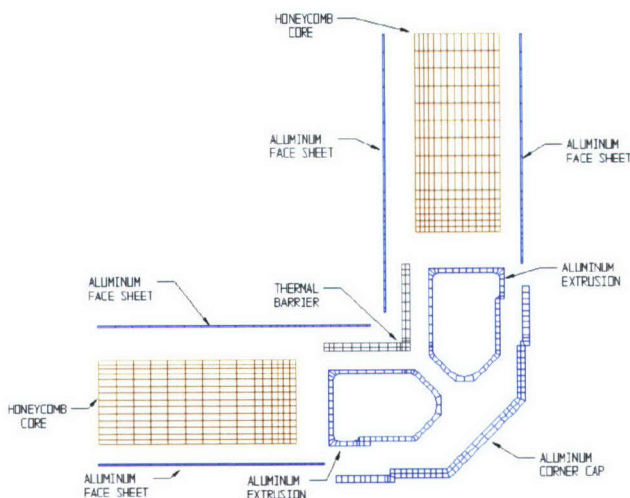
Figure 12. Exploded View of a Typical D-Extrusion Joint

By using a general-purpose structural test frame, welded-steel loading assembly, and hydraulic actuator, two line loads were quasi-statically applied to the shelter side wall using the loading bars as shown in figure 10. A spherical bearing was used to connect the loading assembly to the test frame. Because the bearing was not capable of resisting torques or bending moments, the resultant loads applied along the two load bars were equal. The stiffness of the overall loading assembly prevented deformations of these bars along their lengths; therefore, all points of the shelter section in contact with a specific loading bar deflected the same amount as that particular load bar. It cannot be inferred, however, that deflections under both load bars were equal.

A preliminary FEA model was used to identify locations for positioning up to 76 strain gages. The strain gages were bonded on the inner and outer face sheet surfaces as shown in figure 10. Strain gages 1 and 2 were located at the forward end of the shelter test section; gages 3 and 4 were located at the middle of the shelter test section; and gages 5 and 6 were located at the aft end of the shelter test section. Strain gages 1, 2, and 3 were located on the outer face sheets; gages 4, 5, and 6 were located on the inner face sheet surfaces. All gages were uniaxial and oriented along the shelter hoop direction. Strain data were recorded with a data acquisition system. The center deflections of the side wall and roof panels were recorded using linear variable displacement transducers (LVDTs).

Section test 1 included 72 strain gages located in rows A through L. For this test specimen, the maximum applied load was 9935 lb. Strain measurements at rows D and F were dominated by mostly pure bending behavior but, by contrast, were less than 25% of row E—

suggesting that the D-extrusion joints along the upper and lower side-wall edges transferred less moment than would be expected for rigid connections. This counterintuitive observation rendered the restraining effects of these joints to be rotationally limited; that is, the D-extrusion joints behaved more like pinned connections rather than rigid connections. The rotational stiffness at the wheel well-to-floor joint was comparable to those of the side wall/roof and side wall/wheel-well joints. Displacement readings from the roof and side-wall LVDTs at maximum load were 2.493 inches inward and 0.104 inch outward, respectively. A localized tensile fracture through the floor inner face sheet and the blast hoop stiffener occurred inches forward of the wheel-well region as shown in figure 10. Although some plastic deformation of the side wall was evident, no face sheet/core delaminations or fractures of the honeycomb core were detected.

Section test 2 instrumentation was modified to include additional strain gages located at row M. This row location coincided with the region where fracture occurred in the previous test section. Only four gages were used on this row; they were numbered consistently with those shown in other rows as gages 1 and 4 at the forward end and 3 and 6 at the aft end. The maximum load applied during section test 2 was 10,422 lb, with a tensile fracture of the inner face sheet and hoop stiffener occurring directly through strain gage M3. This failure location was symmetrically opposite that of the first test. At an approximate load of 9806 lb, however, a pair of buckled regions (wrinkles) in the external (compressive side) face sheet occurred because of the contact between the loading bars and the side wall. The buckled regions shown in figure 13 were located immediately adjacent to the inside of the loading bars and were a direct result of excessive friction forces preventing slippage between the load points and the external face sheet.
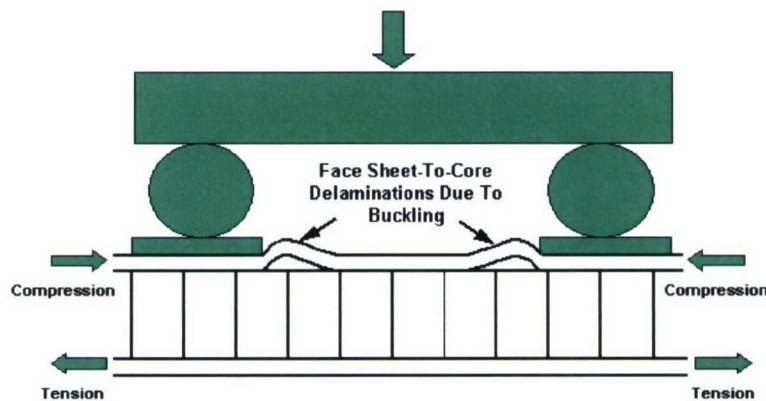
Figure 13. Buckling Failure of the Compressive Face Sheet During Section Test 2

By not allowing slippage to occur, the region of the external face sheet between the loading bars simply acted as a plate on an elastic foundation subjected to an in-plane compressive load. Strain measurements at rows B through G and J through M were bending-dominant; strain measurements at rows A and H were membrane-dominant. The maximum tensile and compressive strain magnitudes for the side wall were nearly identical (indicating pure bending) to 5000 μ in./in.; both occurred at row E and established that significant yielding resulted. Strains at rows D and F were less than 28% of the strain at row E, which indicated that

the D-extrusion joints limited rotational resistance to the applied bending loads. With increasing distance away from the clamping plate assembly, roof strains at rows A through C increased and became more bending-dominant. Wheel-well strain measurements at rows G through I were relatively low (< 800 μ in./in.). Strain values, however, increased locally to a maximum compressive strain of approximately -1200 μ in./in. at row J near the interface of the wheel-well vertical panel and the floor. Floor strains at rows K and L were moderate (up to 1200 μ in./in.) and reflected a flexure-dominant response, as evidenced by the bending deformation of the floor. The maximum roof and side-wall displacements were 2.859 inches inward and 0.051 inch outward, respectively. Strain measurements were consistent with those obtained from the first test. The maximum roof and side-wall displacements were 2.859 inches inward and 0.051 inch outward, respectively. Plastic deformations were evident in the D-extrusions of the roof-to-side-wall and floor-to-side-wall joints, as shown in figure 14, as well as the two localized buckling zones on the outer face sheet of the side wall. There were, however, no delaminations between the face sheets and honeycomb core or fractures of the honeycomb.

Pre-test view   Post-test view
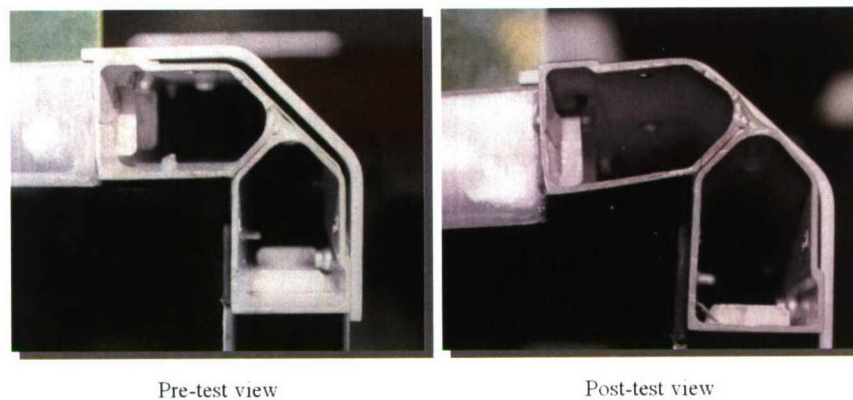
Figure 14. Pre-Test and Post-Test Views of Roof-to-Side-Wall Joint in Representative Structural Testing

Two testing modifications were made for section test 3. Dial indicators were used to measure relative motions at the five locations shown in figure 15 so that changes in joint angles could be calculated. The maximum applied load was 10,441 lb, with a tensile failure of the inner face sheet and hoop stiffener occurring adjacent to the M3 strain gage location. Bending-dominant strains were observed in all rows except A and H. Side-wall strains at row E exhibited a pure bending response up to yielding ($\approx \pm 4{,}000$ μ in./in.). Beyond yield, the maximum strains at this row were 5872 μ in./in. in tension and -4418 μ in./in. in compression. Similar to the previous tests (section tests 1 and 2), maximum strain magnitudes in rows D and F were less than one-third of row E, which also indicated compliance at the D-extrusion joints. Magnitudes of wheel-well strains in rows G through I were less than 680 μ in./in. An increase in wheel-well strains was observed at row J, adjacent to the interface at the floor, with a maximum compressive reading of -1019 μ in./in.. This finding was consistent with those of section tests 1 and 2. Floor strain at rows K and L were approximately 25% higher in compression than in tension but showed a bending dominance. Deflection readings for the LVDTs were 2.574 inches inward for the side wall and 0.058 inch outward for the roof. Post-test inspection revealed no delaminations

16

between the face sheets and honeycomb core and no core fractures. Joint and panel rotation angles were plotted in figure 15 as a function of load. The maximum recorded change in joint rotation angle was –6.3°, which occurred at the roof/side-wall joint at 6950 lb. This load was not, however, the maximum load; it was the load at which the dial indicator slipped and no further measurements at this location were possible. A linear extrapolation predicted that the roof/side-wall joint would have rotated by –7.0° had the dial indicator remained in the proper position. The floor-panel rotation was 19.6° at maximum load.
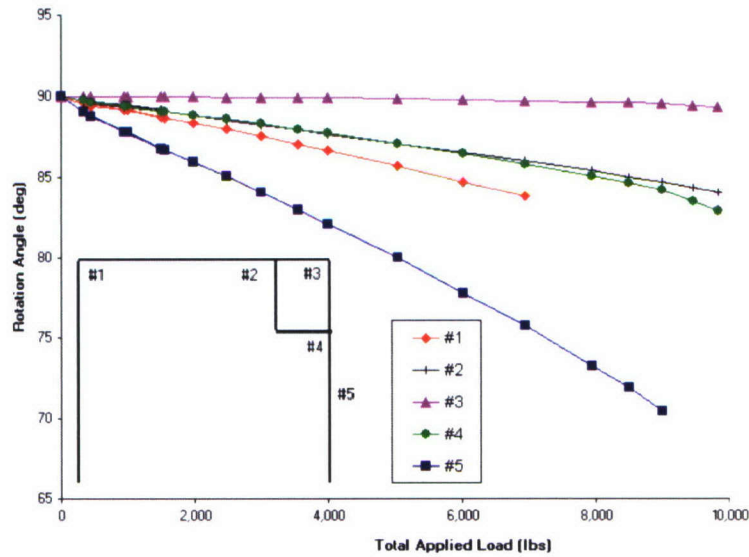
Figure 15. Plot of Measured Rotation Angles Versus Total Applied Load for Section Test 3

Results of the three representative section tests generally indicated that the structural behavior was linear with respect to the applied load. Additionally, the repeatability of the load-displacement curves as shown in figure 16 was indicative of the high-quality manufacturing processes used to fabricate the specimens.
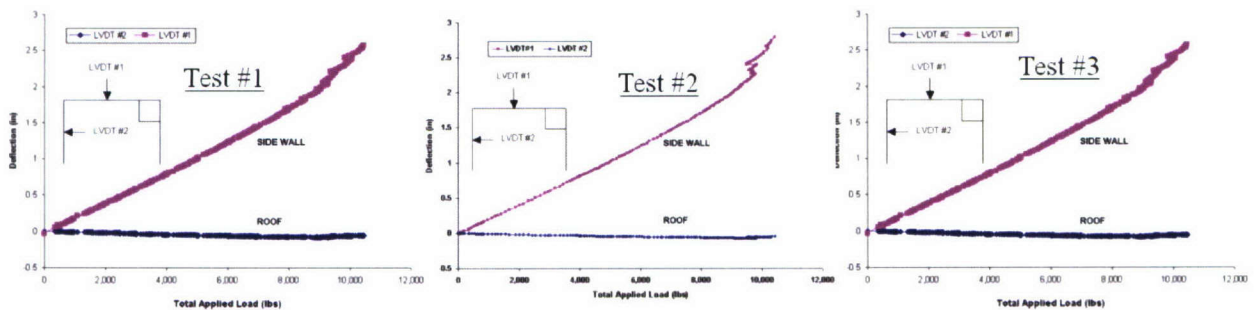
Figure 16. Plot of LVDT Displacement Readings Versus
Total Applied Load for Section Tests 1, 2, and 3

17

Failure modes for all three section tests were identical and occurred at symmetric positions across the floor. Load at failure varied by less than 5% on average. Deflection readings from the roof and side-wall LVDTs were linear up to the onset of yielding at the fracture regions. Strain distributions were also repeatable. All strain gage rows except rows A and H demonstrated bending-dominant responses. Rows A and H, however, were subjected to appreciable membrane strains in comparison to their bending strains. The presence of the membrane strains was indicative of a load stiffening effect that introduced geometric nonlinearities to these particular rows at an approximate total applied load of 5000 lb.

Collectively, the strain results counterintuitively revealed that the D-extrusion joints were rotationally compliant. These joints were originally anticipated to remain rigid; that is, the initially right angles between adjacent panel regions were expected to remain at right angles when loaded. These tests, however, demonstrated that the D-extrusion joints, when subjected to closing moments during flexure, actually behaved more like pinned connections rather than rigid joints in which their rotations were not negligible. The joints contributed only a limited amount of rotational resistance to the flexure loads. The effects of these finite rotations were significant on the resulting strain and deflection responses of the test sections. Furthermore, the limited rotational resistance was expected to have a similar impact on the strain and deflection behavior of the complete shelter.

A linear elastic finite element model of the substructural test specimen (in figure 10) was developed to simulate the section test behavior and to match the experimental strain gage data and the LVDT deflection results. The model included second-ordered sandwich elements for the panels, beam elements for the extrusions, and spring elements for calibrating the joint rotational stiffnesses. A nominal 10,000-lb total load was applied, and the joint rotational stiffnesses were adjusted until the model matched the experimental strain, deflection, and joint rotational angle results.

Table 4 lists the tabulated LVDT and FEA deflection results; the bar graphs in figure 17 show the correlation between the experimental test results and the FEA strain results. These results, however, are for a total applied load of up to only 5000 lb. Beyond this load, the nonlinearities observed at strain gage rows A and H could not be reflected by the linear elastic model.

Table 4. Experimental and FEA Deflections

Deflection Results At 5,000 lb. Total Load (Negative indicates outward)		
	Sidewall	Roof
FEA	0.878	-0.121
Test #1	1.009	-0.079
Test #2	0.809	-0.105
Test #3	1.014	0.055
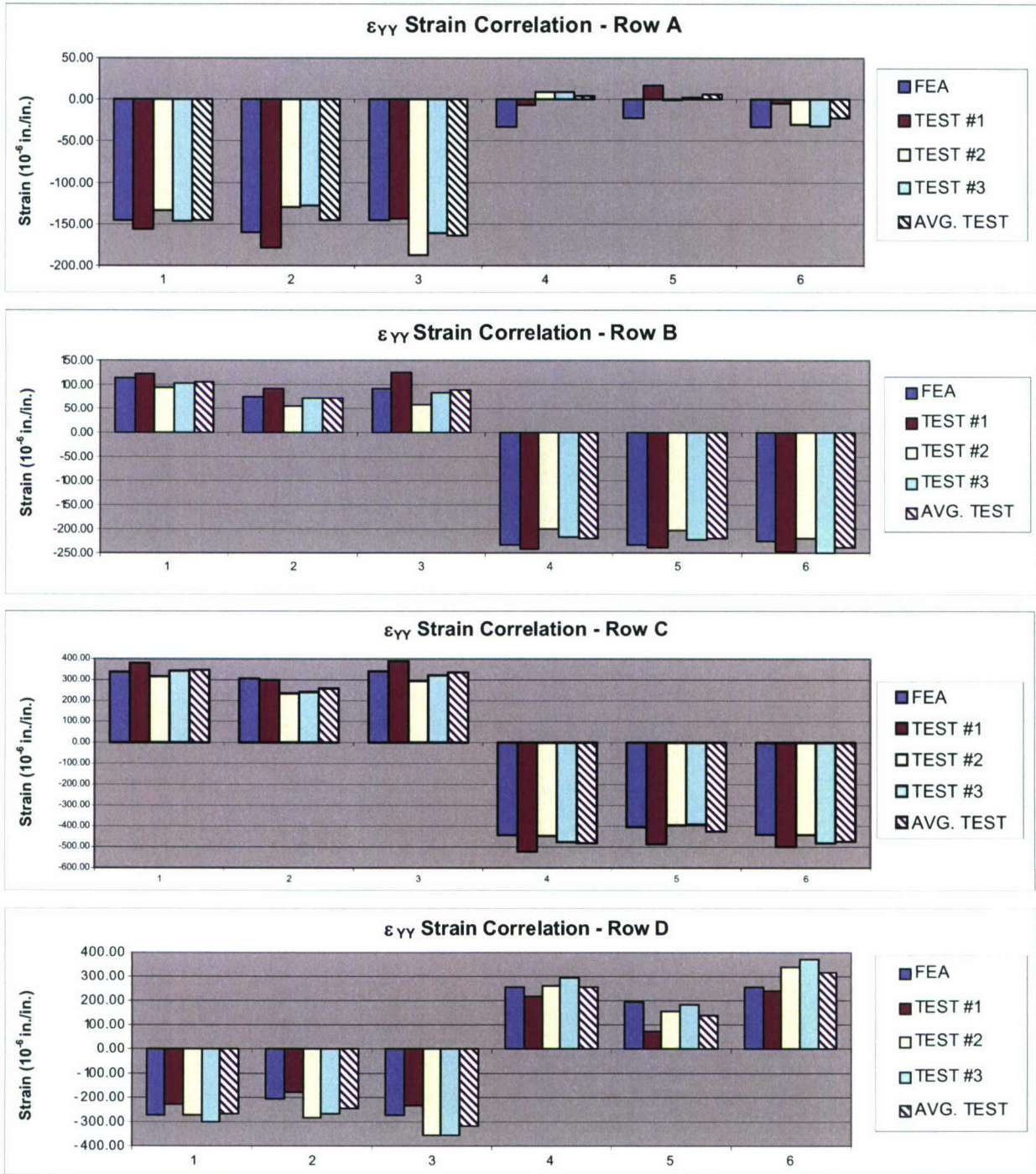
Figure 17. Comparison of Experimental and FEA ε_{yy} Strains for Gage Rows A Through M
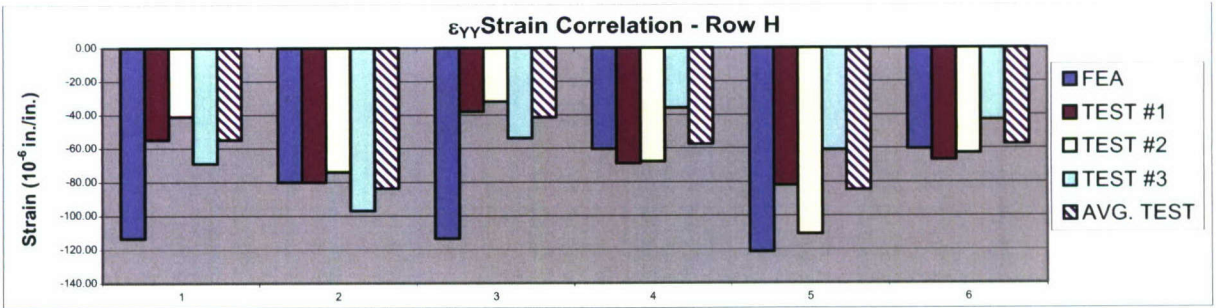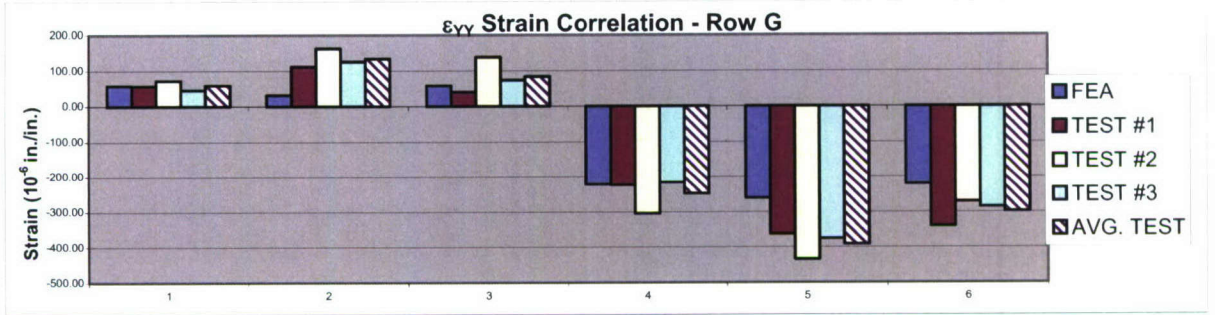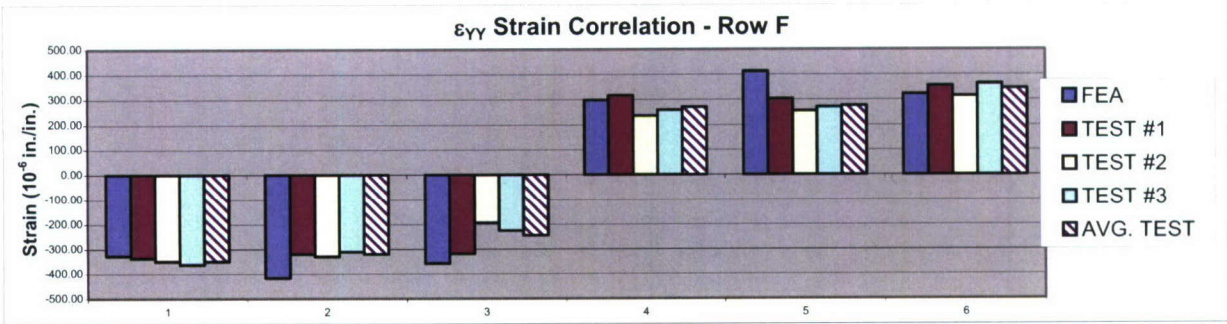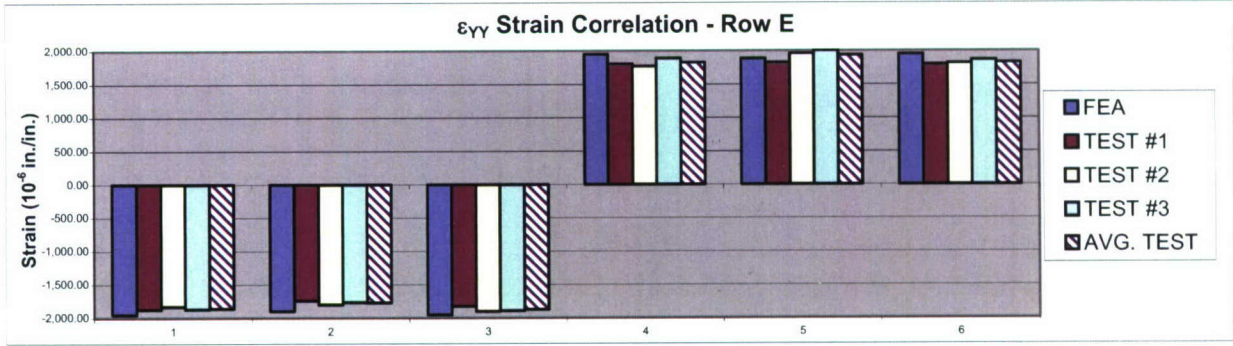
Figure 17. Comparison of Experimental and FEA ε_{yy} Strains for Gage Rows A Through M (Cont'd)
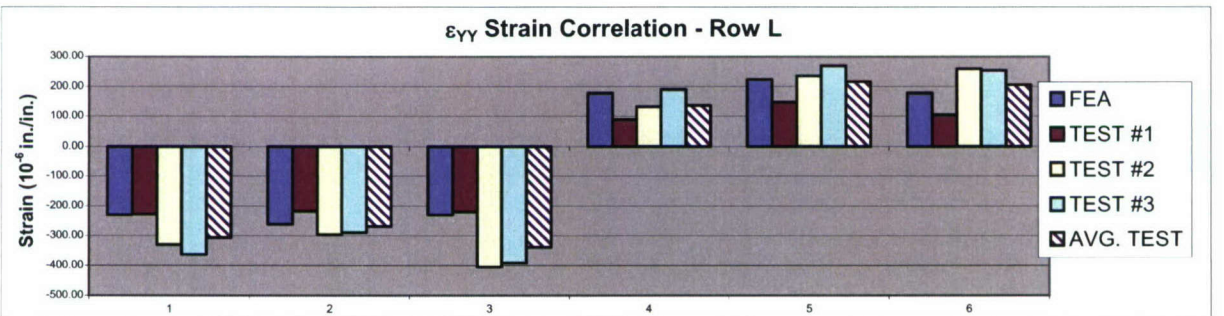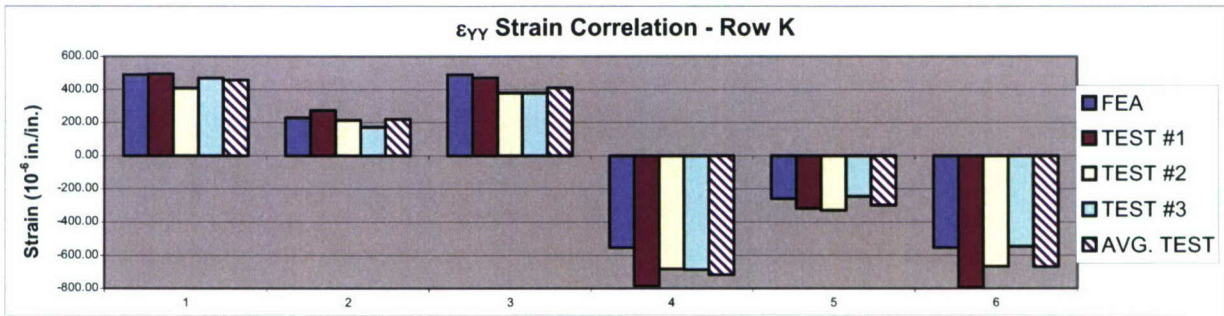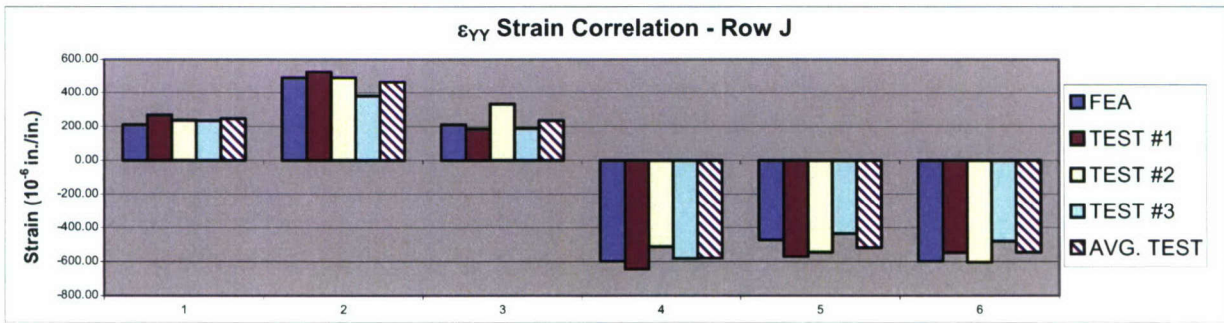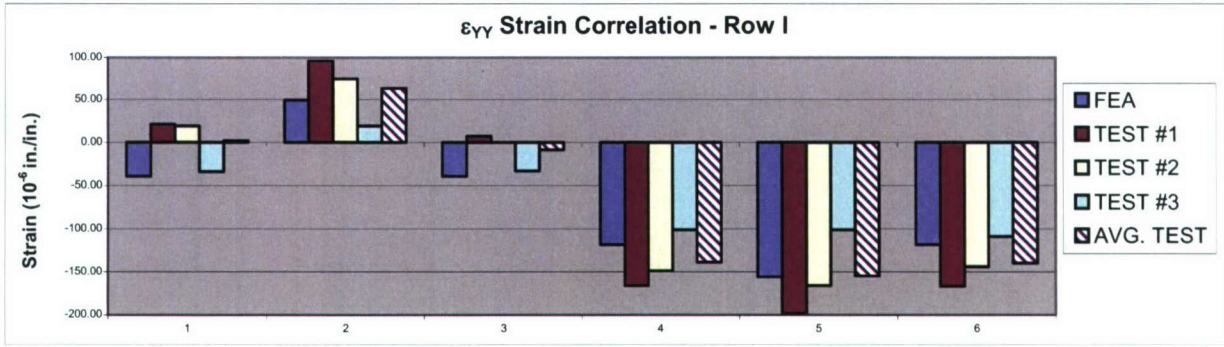
*Figure 17. Comparison of Experimental and FEA ε_{yy} Strains
for Gage Rows A Through M (Cont'd)*
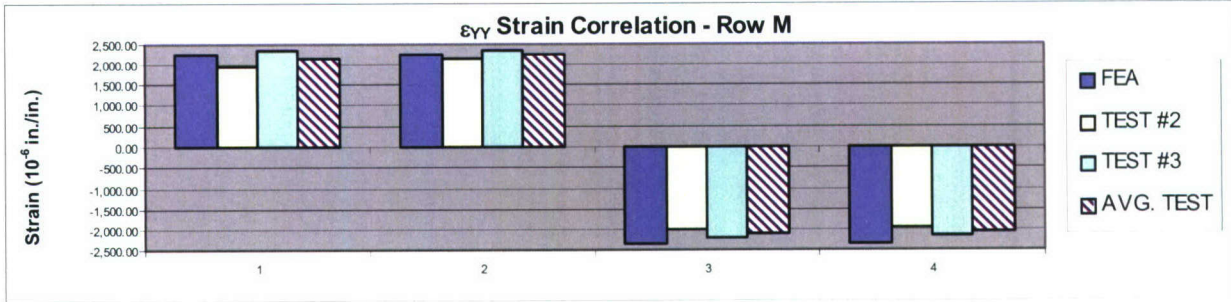
***Figure 17. Comparison of Experimental and FEA ε_yy Strains
for Gage Rows A Through M (Cont'd)***

The bar charts comparing experimental and predicted strains shown in figure 17 generally demonstrated a high level of correlation. The joint rotational stiffnesses, K_{ROT}, that were used in the FEA model are shown in table 5. These stiffnesses provided the calibration necessary to achieve the correlation of strain and deflection results between the tests and the model.

Table 5. Section Test Joint Rotational Stiffnesses

Joint Location Description	K_{ROT} (in-lb/rad)
Roof To Side Wall	2,500
Side Wall To Wheel Well	2,500
Wheel Well To Floor	2,500
Side Wall To Floor	5,000
Wheel Well Horizontal To Floor	2,500
Side Wall To Vertical Wheel Well	5,000
Floor To Wheel Well Fore & Aft	2,500
Clamped Edges	55,000

22

Figure 18 plots the nodal force distributions resulting from the transfer of loads from the loading bars to the side wall. This plot exhibited stiffening effects from the blast hoop extrusions, as demonstrated by the locations of relative peak forces being coincident with the extrusion positions. Similarly, figure 19 plots the hoop force reactions at the nodes along the clamped roof and floor edges. The variations of these reaction forces also demonstrated a stiffening effect in the presence of the blast hoop extrusions. The roof-edge reactions were approximately 300% greater than the floor-edge reactions, which explained why the roof strain gages at row A signified a pronounced state of membrane stresses. The two fixed-point restraints on the floor adjacent to the wheel wells reduced the in-plane loading within the floor.
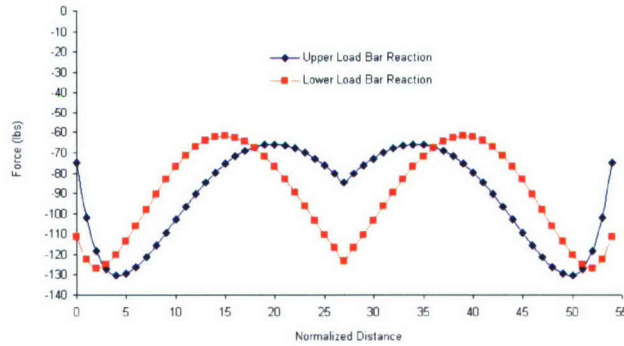
Figure 18. Plot of Model-Predicted Nodal Forces Along Upper and Lower Load Bars
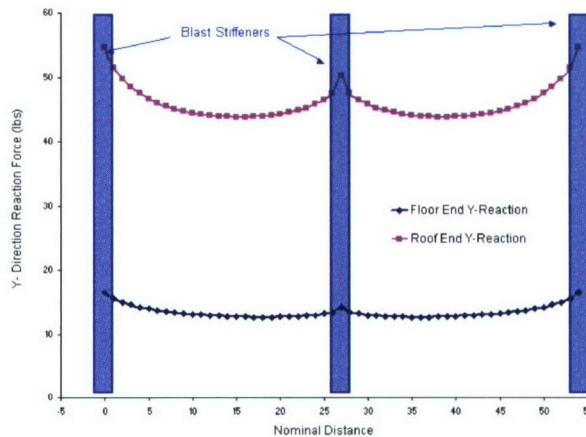
Figure 19. Plot of Model-Predicted Global Y-Direction Reaction Forces at Floor and Roof Edges

Stress contour plots of the inner and outer face sheets and honeycomb layers were captured in accordance with the element local material directions (that is, the X- and Y-axes as shown in figure 20) and are shown in figures 21 through 26. Figures 27 and 28 show the global displacement contour plots. A contour plot of the strain energy developed in the model at full loading is shown in figure 29. Note that the location of maximum strain energy reflects the failure locations observed during testing.

23
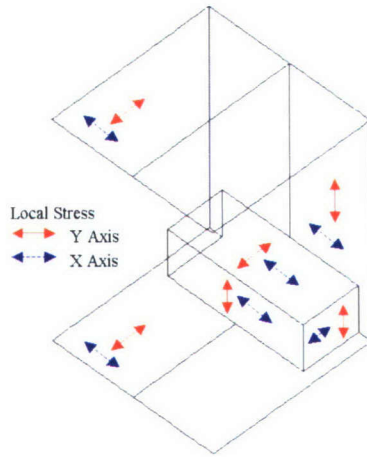
Figure 20. Sandwich Element Local Stress Output Axes
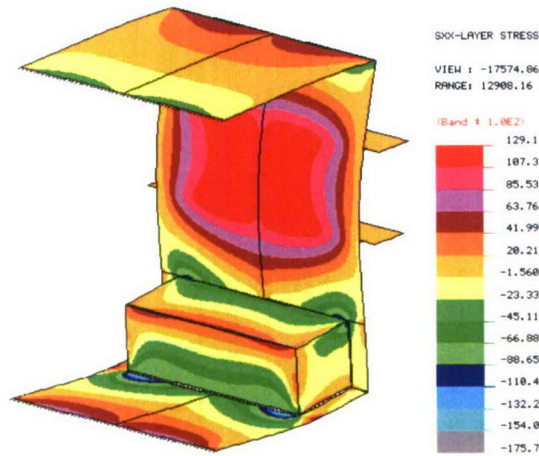
Figure 21. Contour Plot of Longitudinal Stress σ_{xx} for Inner Face Sheet of Section Test
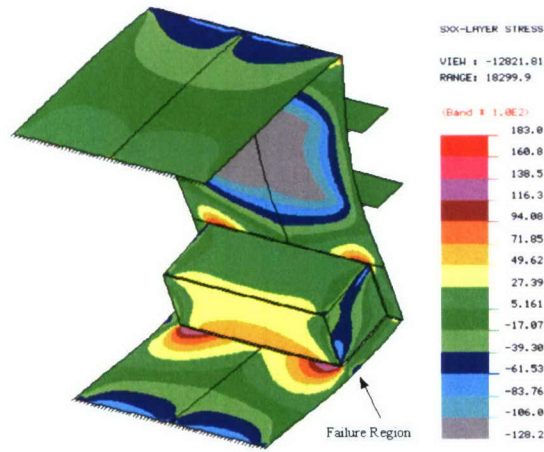
Figure 22. Contour Plot of Longitudinal Stress σ_{xx} for Outer Face Sheet of Section Test

24
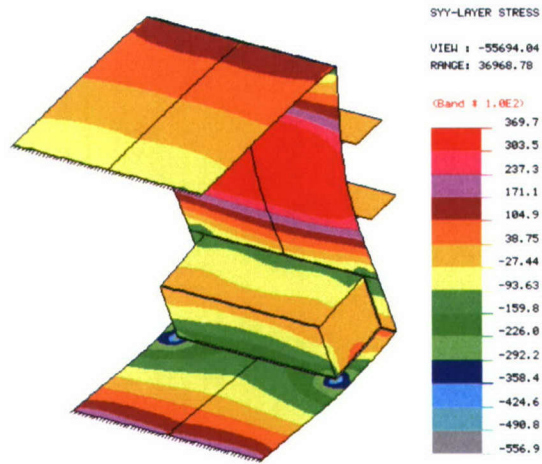
Figure 23. Contour Plot of Hoop Stress σ_yy for Inner Face Sheet of Section Test
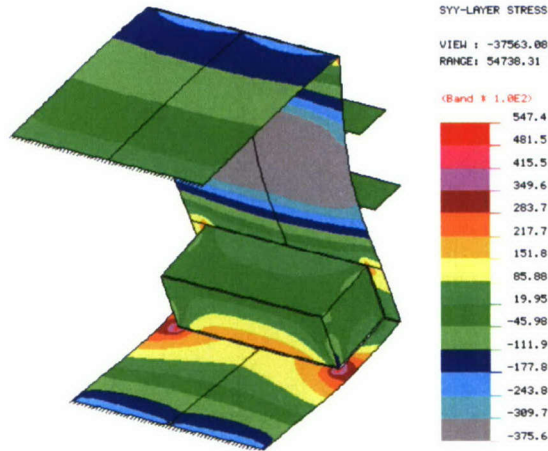
Figure 24. Contour Plot of Hoop Stress σ_yy for Outer Face Sheet of Section
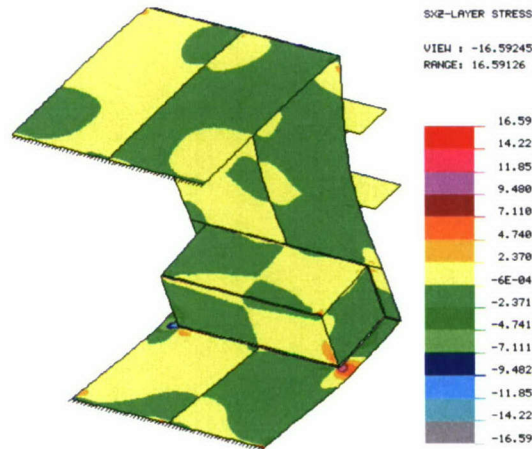
Figure 25. Contour Plot of Transverse Shear Stress σ_xz for Honeycomb Core of Section Test

25
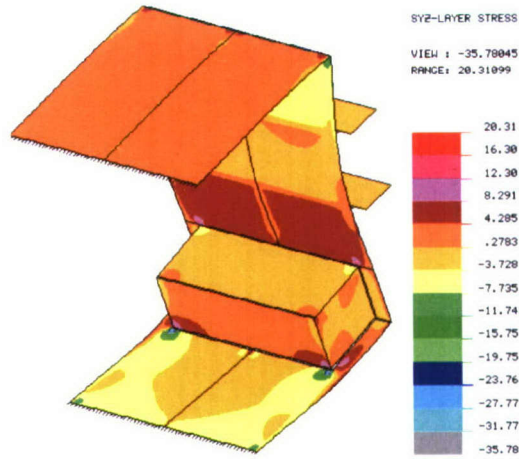
Figure 26. Contour Plot of Honeycomb Core Transverse Shear Stress σyz for Section Test
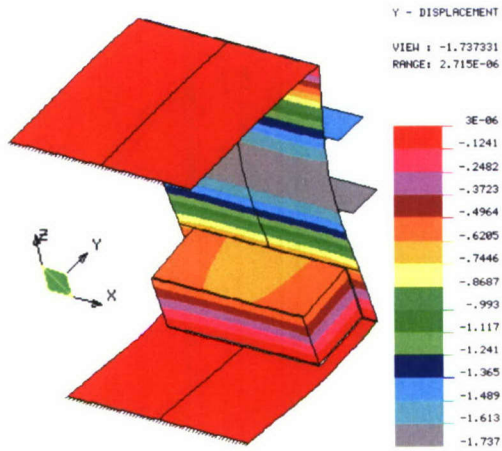
Figure 27. Contour Plot of Lateral Displacements Uy for Section Test
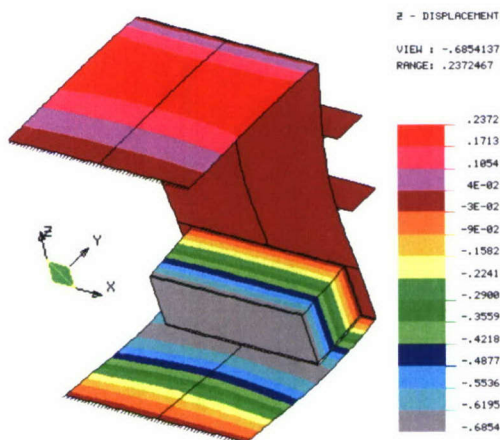
Figure 28. Contour Plot of Vertical Displacements Uz for Section Test

STRAIN ENERGY

VIEW :-7.450E-06
RANGE: 6.002105

16.20
15.05
13.89
12.73
11.57
10.42
9.259
8.102
6.944
5.787
4.629
3.472
2.315
1.157
-7E-06
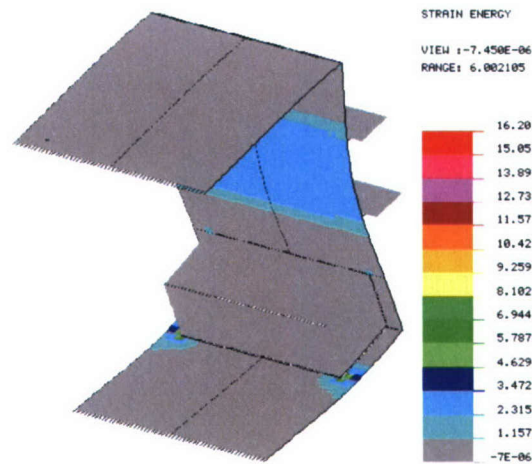
Figure 29.   Contour Plot of Strain Energy for Section Test

To further increase the structural integrity of the shelter, another key modification was included. The major joints formed by the D-extrusions found in a previous-generation shelter possessed unequal (bilinear) rotational stiffnesses when they were subjected to an opening versus a closing moment because of the presence of only a single weld. By adding an internal weld between the inner face sheets, the current shelter joints possessed equal rotational stiffnesses for both opening and closing moments.

The difference in the joint rotational stiffnesses is explained in the plane strain joint models shown in figures 30, 31, and 32.

SYMMETRY
DISPLACEMENT
CONDITIONS ALONG
THIS EDGE

PRESSURE
DISTRIBUTION
ALONG THIS EDGE

ROOF/SIDEWALL JOINT MODEL
PLANE STRAIN CASE WITH
STATIC PRESSURE LOAD

NOTE SHEAR DEFORMATION
IN THERMAL BARRIER LAYER

FIXED
DISPLACEMENT
CONDITIONS
ALONG THIS EDGE
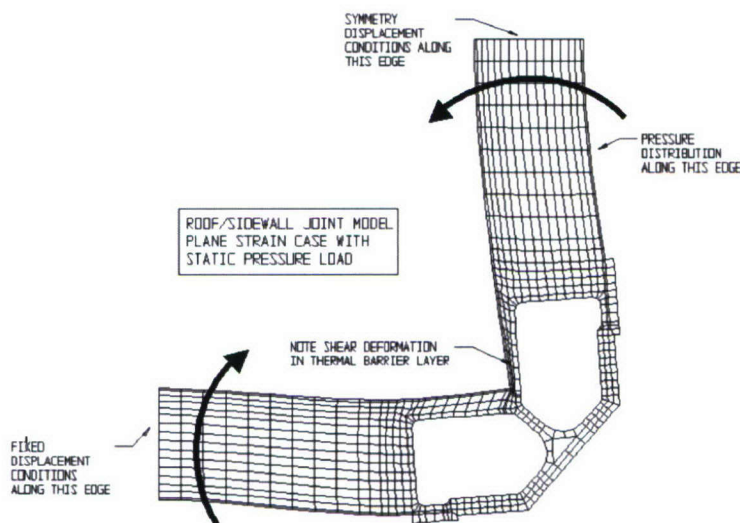
Figure 30.   D-Extrusion Joint Subjected to Closing Moment
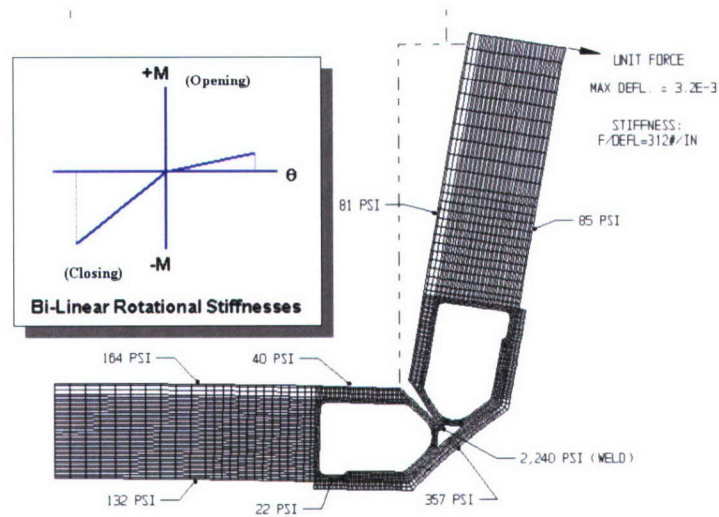
***Figure 31. Bilinear Rotational Stiffnesses: Opening Versus Closing
Moments for D-Extrusion Joints***
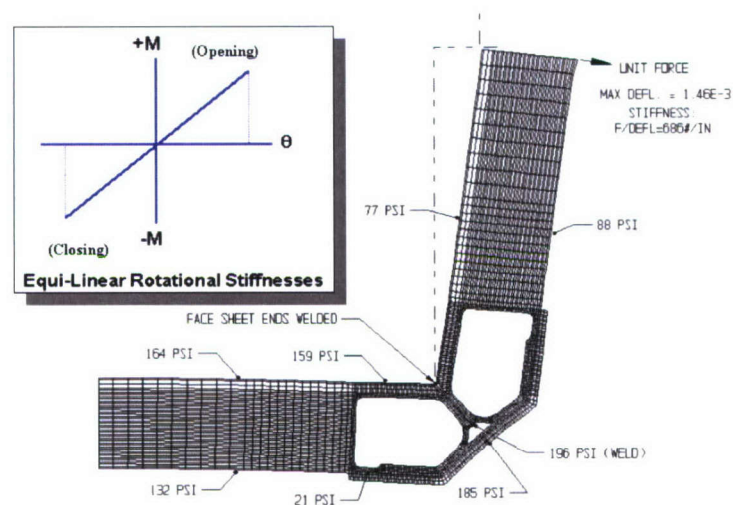
***Figure 32. Equilinear Rotational Stiffnesses: Opening Versus Closing
Moments for D-Extrusion Joints***

These models were subjected to a horizontal unit load applied at the top of the vertical member and supported by fixed constraints imposed on the left end of the horizontal member as shown. The applied unit load generates an opening moment within both joints. Stress values shown represent Von Mises stresses at key locations within the aluminum components including the external weld. It is clearly apparent that the doubly welded joint design provides a more uniform stress distribution, significantly reduces the peak stresses, and gains a 2:1 increase in joint rotational stiffness. Although the section tests were conducted with joints containing only the external welds, the results are expected to match those for a doubly welded joint section test subjected to the same loading because all the joints in the section test experienced closing moments. Joints constructed without the internal welds and subjected to closing moments

experience contact between the joint extrusions, resulting in a kinematic stiffening effect. Conceivable load cases in which a complete shelter may experience opening moments at these joints include all dynamic loading events and static loading events, such as external air transport (EAT) lift, deadweight, and racking tests.

As a result of the plastic deformations observed in the D-extrusion joints during the representative structural tests, a modification was made by adding a diagonal rib to stiffen it against collapse. This modification is shown in figure 33 and will be used in the production of future shelters.
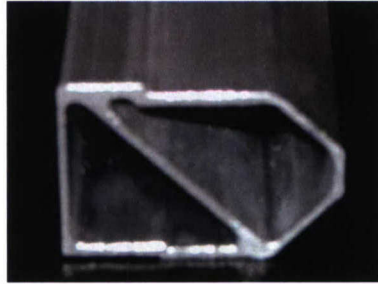
Figure 33. Rib-Stiffened D-Extrusion Design

SHELTER MODEL FOR MODAL AND DYNAMIC LOAD CASES

A complete structural model of the shelter was developed (see figures 34 and 35). This model included all sandwich panel sections, extrusions, joint rotational stiffnesses, and rigid boundary conditions that simulated the shelter-to-vehicle mounting attachments. Each of these was required for predicting the response of the full shelter to various loading events when the shelter was mounted to the HMMWV. Rigid link elements were used to represent the hinges and the striker mechanisms connecting the door panel to the door-end wall. The demarc panel (access panels used for signal or power input/output points) elements were connected to the sandwich elements and closeout extrusions by using rigid links. Second-ordered sandwich elements and linear beam elements, as used in the model of the representative shelter test sections, were used for the full shelter model.
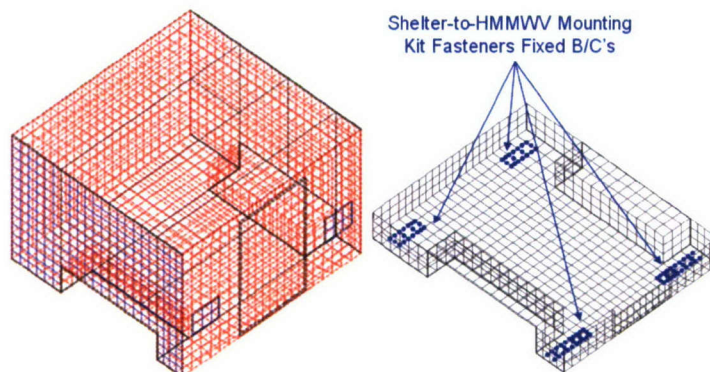
Figure 34. FEA Model of the Full Shelter
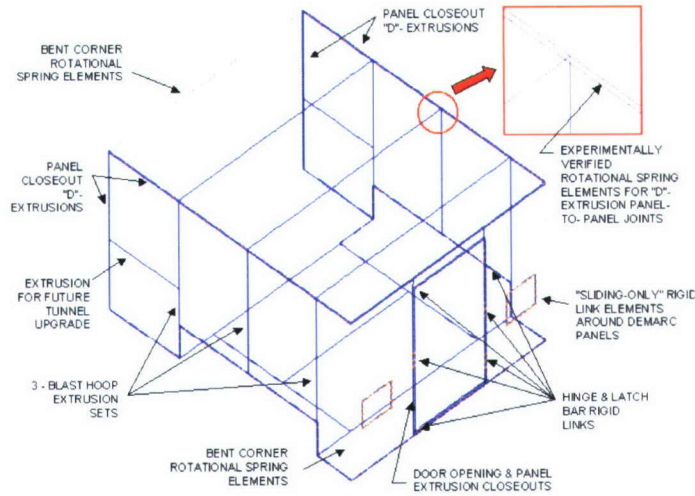
Figure 35. Description of Beam, Spring and Rigid Link Elements

MODAL AND DAMPING ANALYSES

For dynamic loading events, the time-based equations of motion shown in equation (8) included effects caused by damping. The damped behavior of the shelter was determined by conducting an eigenvalue analysis that established natural frequencies of vibration (*fi*) and corresponding mode shapes so that proper values of damping could be established. Let

$$[M]\underline{\ddot{X}} + [C]\underline{\dot{X}} + [K]\underline{X} = \{f(t)\},$$
(8)

where   [M]   =   global mass matrix,

         [C]   =   damping matrix,

        {f(t)}   =   vector of nodal forces,

         [K]   =   global stiffness matrix,

         $\underline{X}$ =   vector of nodal displacements,

         $\underline{\dot{X}}$ =   vector of nodal velocities,

         $\underline{\ddot{X}}$ =   vector of nodal accelerations.

Rayleigh damping[8] (also known as proportional damping) was assumed in accordance with equation (9), which reflects contributions from both mass-based damping α and stiffness-based damping β. In general, stiffness-based damping results from hysteretic effects observed during cyclic loading of elastic materials. Additional sources of structural damping were expected from the mechanically fastened joints and the face sheet/honeycomb core adhesive layers. Mass-based damping affected the dynamic response at lower frequencies; structural-based damping affected dynamic response at higher frequencies. A recommended critical damping ratio ζ of 5% was used for all flexure modes.

$$[C] = \alpha[M] + \beta[K],\tag{9}$$

where
$$\alpha = \frac{2\omega_i\omega_j}{\omega_j^2 - \omega_i^2}\left(\omega_j\zeta_i - \omega_i\zeta_j\right),\tag{10}$$

$$\beta = \frac{2}{\omega_j^2 - \omega_i^2}\left(\omega_j\zeta_j - \omega_i\zeta_i\right),\tag{11}$$

$$\omega_i = 2\pi f_i, \quad \zeta = \frac{C}{C_{cr}}, \quad \zeta_i = \zeta_j = 0.05.\tag{12}$$

The eigenvalue analysis was performed using the Lanczos method[8] with an upper cutoff frequency (f_c) of 100 Hz. The computed mode shapes (eigenvectors) were all flexure dominant with symmetric and antisymmetric deformations. The fundamental natural frequency f_1 was a symmetric flexure mode of the roof at 30.45 cycles/sec (Hz). The first 20 resonant frequencies were spaced rather uniformly and are listed in table 6, along with their corresponding mode shapes. Plots of the first four mode shapes are shown in figure 36. By using values of $\omega_1 = 191.32$ rad/sec and $\omega_2 = 227.33$ rad/sec corresponding to f_1 and f_2, respectively, α and β were computed as $\alpha = 10.389$ and $\beta = 2.389 \times 10^{-4}$.

***Table 6. Frequency and Mode Shape Results Where λ Equals
One Wavelength of a Representative Sinusoid***

Mode #	Frequency (Hz)	Mode Description
1	30.45	Roof - $\lambda/2$ length by $\lambda/2$ width
2	36.18	Curb/road side wall - $\lambda/2$ length by $\lambda/2$ height
3	40.38	Front end wall - $\lambda/2$ width by $\lambda/2$ height
4	45.10	Floor - $\lambda/2$ length by $\lambda/2$ width
5	50.14	Front end wall - $\lambda/2$ width by $\lambda/2$ height
6	56.78	Curb/road side wall - $\lambda/2$ length by $\lambda/2$ height
7	58.73	Door end wall - $\lambda/2$ width by $\lambda/2$ height
8	60.36	Floor - $\lambda/2$ length by $\lambda/2$ width
9	63.58	Roof - λ length by $\lambda/2$ width
10	75.14	Curb/road side wall - $\lambda/2$ length by $\lambda/2$ height
11	79.46	Curb/road side wall - λ length by $\lambda/2$ height
12	83.03	Roof - $\lambda/2$ length by λ width
13	83.51	Door end wall - λ width by $\lambda/2$ height
14	84.10	Curb/road side wall - λ length by $\lambda/2$ height
15	87.58	Curb side wheel well - rotation
16	93.57	Front end wall - λ width by $\lambda/2$ height
17	97.60	Floor - λ length by $\lambda/2$ width
18	102.87	Floor - $\lambda/2$ length by $\lambda/2$ width
19	108.85	Roof - $3\lambda/2$ length by $\lambda/2$ width
20	109.57	Roof - λ length by λ width
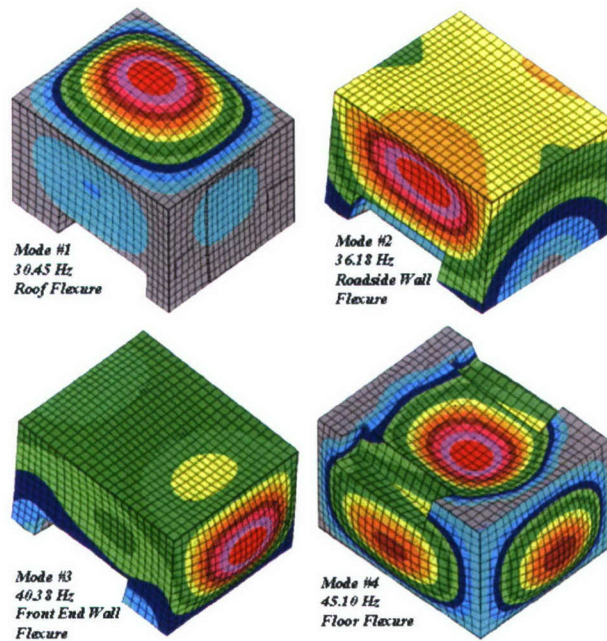
**Figure 36. Modal Analysis Results of First Four Resonant Frequencies
and Corresponding Mode Shapes**

AIR BLAST OVERPRESSURE ANALYSIS

Virtual verification of structural response levels (that is, deflections, stresses, etc.) was necessary for the dynamic blast loading events. Virtual verification also minimized the number of full-scale shelter prototypes required for blast testing. A blast overpressure case, in which the shelter was assumed mounted to a HMMWV, was considered, using the finite element method. This blast case used a nominal 2.5-psi overpressure with the road-side wall as the incident blast face. A blast analysis for only one side-wall was performed because the lateral symmetry of the shelter eliminated the need to perform a separate blast analysis for each side-wall. The floor was considered isolated from air blast overpressure loads because the vehicle cargo area floor would deflect these loads. The front-end wall was not considered as an incident blast face because it was shielded, to a limited extent, by the vehicle cab. The roof was not considered as an incident blast face because the shelter was not designed to support direct overhead air blasts.

This specific overpressure was assumed to be caused by a conventional weapon air blast. Previous analyses by Frantz, et al.[9] concluded that the peak shelter response of a vehicle-mounted shelter subjected to overpressure loads was decoupled from that of the vehicle. Because the blast overpressure pulses were of such short duration, the shelter peak response would occur prior to the vehicle peak response. The vehicle was effectively represented by the rigid boundary conditions at the mounting kit fastener locations shown in figure 34. The displacement results of the shelter blast models were, therefore, considered to be relative with respect to the vehicle.

The blast case was for a 2.5-psi peak side-on overpressure, p_{so}, impinging upon the road-side wall of an empty (nonintegrated) shelter. The road-side wall was assumed to be perpendicular to the propagating direction of the shock wave. Transient pressure-versus-time curves were generated for each surface of the shelter in accordance with procedures outlined by Harris and Crede[10] for a closed box-like structure. At the arrival time $t_a = 0$ the time-varying side-on overpressure $ps(t)$ was a maximum at p_{so} and then decayed exponentially according to equation (13).

$$p_s(t) = p_{so}\left(1 - \frac{t}{t_o}\right)\exp\left(-\frac{t}{t_o}\right),$$ (13)

where t_o = time duration of positive side-on overpressure = 0.789 second, or

$$p_s(0) = p_{so} = 2.5 \text{ psi.}$$

Also, an exponentially decaying reflected pressure $p_r(t)$ was generated by the overpressure wave on the road-side wall reaching a maximum value $p_r(0)$, at time = t_a according to equation (14).

$$p_r(t) = p_s(t)\left(2 + \frac{6 p_s(t)}{7 p_o + p_s(t)}\right),$$ (14)

where p_o = ambient pressure = 14.7 psi ,
$p_r(0) = p_{ro}$ = 5.356 psi.

As a result of the moving air mass, an exponentially decaying dynamic pressure wave $p_d(t)$ developed and is described by equation (15):

$$p_d(t) = p_{do}\left(1 - \frac{t}{t_{od}}\right)^2 \exp\left(-\frac{2t}{t_{od}}\right),$$ (15)

where p_{do} = peak dynamic pressure = 0.15 psi,
t_{od} = time duration of positive dynamic pressure = 1.5 t_0 = 1.183 seconds.

The effective transient pressure loading curve for the road-side wall as the incident blast face p_{bface} was formulated by superimposing the overpressure, reflected pressure, and the dynamic pressure in accordance with equations (16):

$$p_{bface} = \begin{Bmatrix} p_{ro} \\ p_d + p_s \\ p_s \\ 0 \end{Bmatrix} \text{ corresponding to: } time = \begin{Bmatrix} 0 \\ t_c \\ 2\dfrac{t_d}{3} \\ t_d \end{Bmatrix},$$ (16)

33

where t_c = time for the reflected pressure to clear incident blast face = 0.006 second.
t_d = duration of side-on overpressure = 0.592 second.

At t_a, the effective blast face pressure was at its maximum value p_r and decayed to a combined value of overpressure and dynamic pressure at the clearing time t_c. The duration of the reflected pressure t_c equals $3v_o/a$, where a is the distance from the center of the blast face to the nearest edge and v_o is the velocity of the shock wave in air given by equation (17).

$$v_o = 1{,}117 \sqrt{1 + \frac{6p_{so}}{7p_o}} = 14{,}352 \text{ in./sec.} \tag{17}$$

The nonincident shelter surfaces, such as the roof, front-end wall, door-end wall, and curb-side wall, were subjected to only the overpressure as described in equation (14). There were no reflected pressures on these surfaces. The pressure loading arrival times for the roof, front-end wall, and door-end wall were equal to t_a. The arrival time for the curb-side wall pressure loading, however, was delayed by $\Delta t_a = L/v_o$. Here, L represents the separation distance between the incident blast face (road-side wall) and the opposite face (curb-side wall) and was equal to the width of the shelter. This delay represented the time required for the pressure wave to traverse across the roof before loading of the curb-side wall began. The time increment needed to fully pressurize the curb-side wall Δt_p was $5a/v_o$. The effective transient pressure loading for the curb-side wall p_{opface} was formulated by superimposing contributions from the overpressure and dynamic pressure as shown in equation (18).

$$p_{opface} = \left\{ \begin{array}{c} 0 \\ 0 \\ (p_s - 0.5p_d)\left(\dfrac{L+5a}{v_o}\right) \\ (p_s - 0.5p_d)\left(\dfrac{L}{v_o} + 2\dfrac{t_d}{3}\right) \\ 0 \end{array} \right\} \text{ corresponding to: } time = \left\{ \begin{array}{c} 0 \\ \dfrac{L}{v_o} \\ \dfrac{L+5a}{v_o} \\ \dfrac{L}{v} + 2\dfrac{t_d}{3} \\ \dfrac{L}{v_o} + t_d \end{array} \right\}. \tag{18}$$

A plot of the effective transient pressure curves resulting from an air blast impinging upon the road-side wall is shown in figure 37. Figure 38 shows the transient shelter pressures for road-side wall as the incident blast face (P_{so} = 2.5 psi).

34
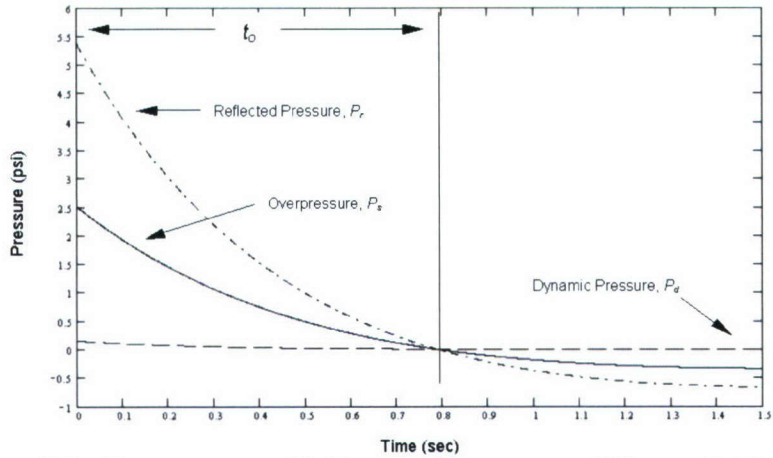
**Figure 37. Overpressure, Reflected Pressure, and Dynamic Pressure
Versus Time Curves for P_{so} = 2.5 psi**

**Figure 38. Transient Shelter Pressures for Road-Side Wall as the
Incident Blast Face, P_{so} = 2.5 psi**

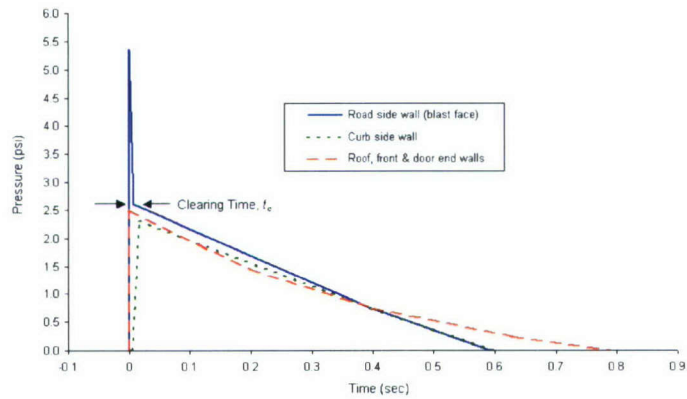A graphic representation of the transient pressure distributions is shown in figure 39 for the road-side wall as the incident blast face.
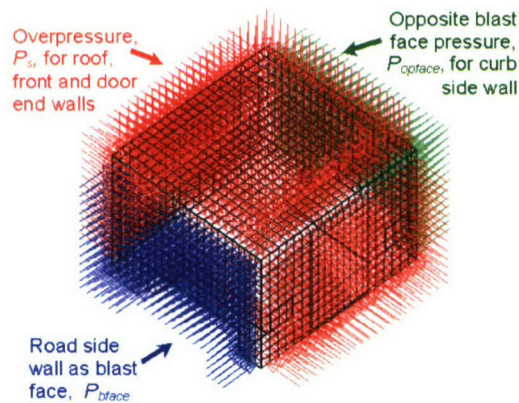

Figure 39. Surface Pressures for Road-Side Wall as the Incident Blast Face

The transient solution was obtained through direct integration of the linear equations of motion using the implicit Newmark integration method described by Bathe[8] and shown in equation (19).

$$M\,^{t+\Delta t}\ddot{U} + C\,^{t+\Delta t}\dot{U} + K\,^{t+\Delta t}U = \,^{t+\Delta t}R. \tag{19}$$

Initial conditions of displacement ^{o}U, velocity $^{o}\dot{U}$, and acceleration $^{o}\ddot{U}$ were prescribed as zero at $t = 0$. The displacements and velocities were enforced for equilibrium at time $t + \Delta t$ according to equations (20 and 21):

$$^{t+\Delta t}\dot{U} = \,^{t}\dot{U} + \left[(1 - \delta)\,^{t}\ddot{U} + \delta\,^{t+\Delta t}\ddot{U}\right]\Delta t. \tag{20}$$

$$^{t+\Delta t}U = \,^{t}U + \,^{t}\dot{U}\Delta t + \left[(1/2 - \alpha)\,^{t}\ddot{U} + \alpha\,^{t+\Delta t}\ddot{U}\right]\Delta t^{2}. \tag{21}$$

Here, Δt is the time step for integration and the parameters δ and α were set to 0.5 and 0.25, respectively, so that the Newmark method was unconditionally stable, thus preventing unbounded round-off errors. Proper selection of Δt controlled which frequencies and mode shapes were allowed to participate in the desired solution. In general, an accurate solution is obtained when $\Delta t < 0.05\,\tau_{c}$ where τ_{c} = the smallest natural period considered. Using the cutoff frequency f_{c} = 100 Hz, τ_{c} was computed as 0.01 second and Δt was 0.5 millisecond. The blast solution was computed for $0 \le t \le 0.9$ second, which captured the peak and overall responses of each shelter surface.

Results of the blast analysis, with the road-side wall as the incident blast face and Pso = 2.5 psi, established that the peak lateral displacement (global Y-direction) of the road-side wall center node was 2.119 inches, which occurred at time t = 8 milliseconds. Figure 40 shows the resultant square root sum of squares (SRSS) displacement contours for the full shelter at this time. Graphs of the displacement-time histories for the global X-, Y-, and Z-directions are shown in figures 41 and 42. Figure 41 uses a short-duration time scale of 0.1 second to clearly exhibit the arrival time t_{a}; figure 42 shows the entire response spanning up to 0.9 second.
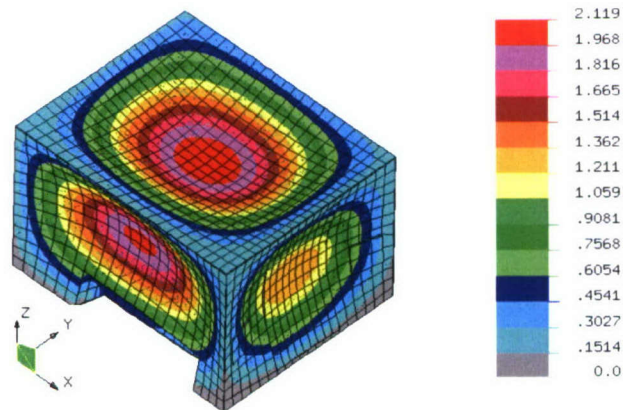
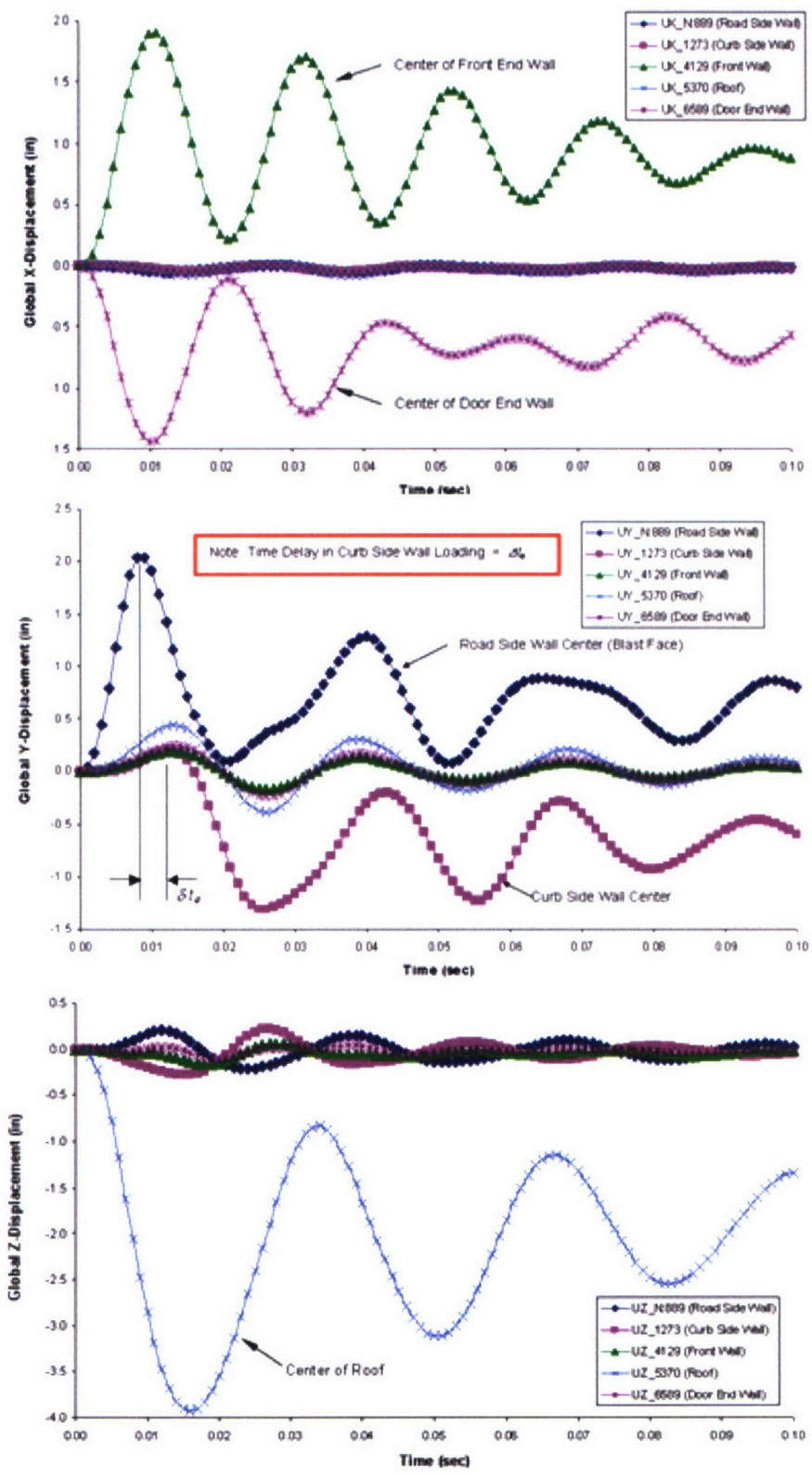***Figure 40. Displacement Contour Plot at Time of Peak Road-Side Wall Displacement (t = 8 ms)***

Figure 41. Global X- , Y- , and Z-Displacement Time History Curves of Shelter for Road-Side Wall Blast with P_{so} = 2.5 psi Shown on a 10-Millisecond Time Scale
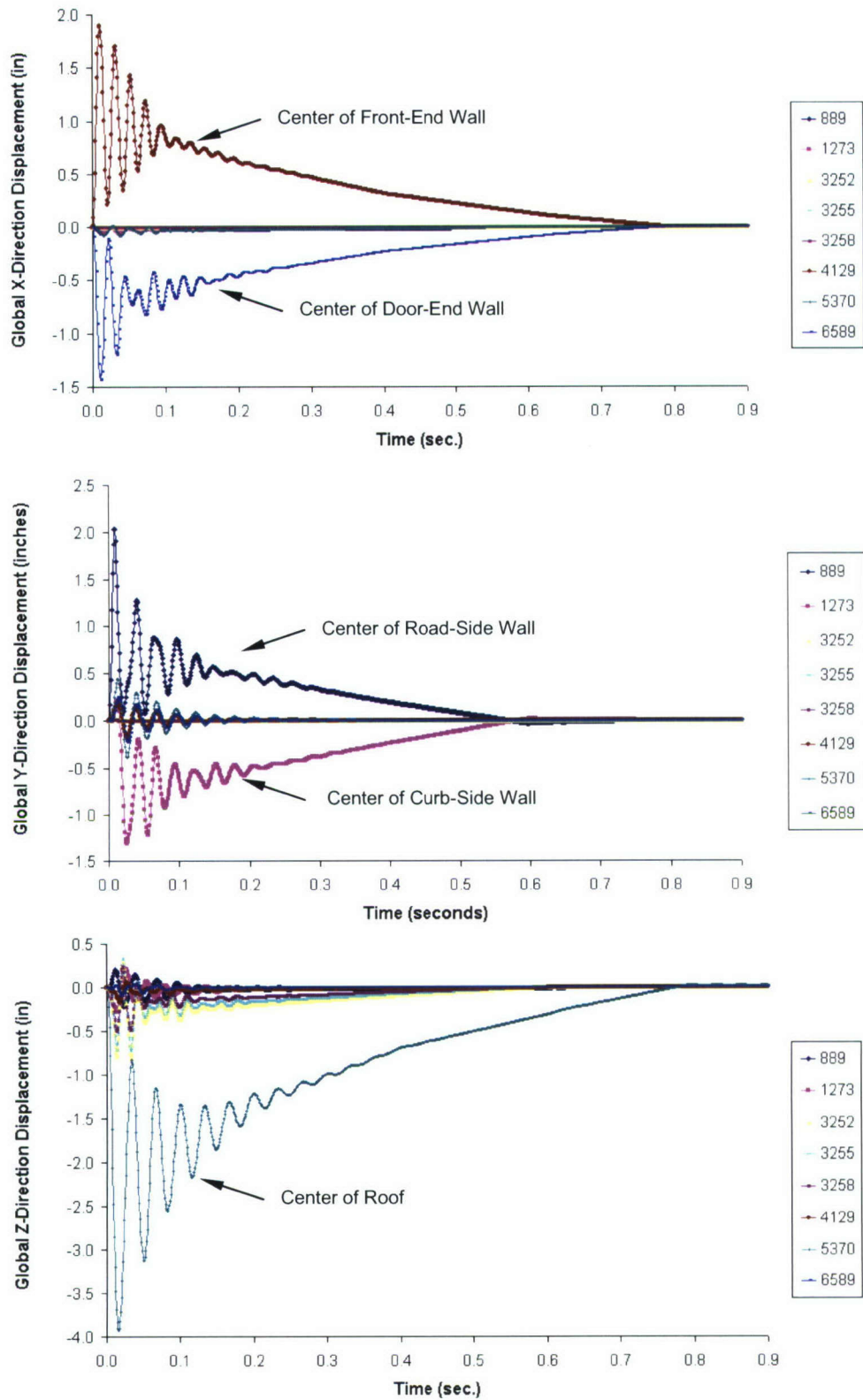
Figure 42. Global X- , Y- , and Z-Displacement Time History Curves of Shelter for Road-Side Wall Blast with P_{so} = 2.5 psi Shown for Entire 90-Millisecond Time Response

Figure 43 depicts the shelter deformations corresponding to a cross section through the central hoop stiffener at key response times. The peak lateral displacement of the curb-side wall center node (global Y-direction) was –1.311 inches, which occurred at t = 24 milliseconds. Peak lateral displacement of the roof center node (Z-direction) was –3.961 inches, which occurred at t = 15 milliseconds. Peak lateral displacements for the front-end and door-end walls were 1.901 inches and 1.435 inches, respectively, which occurred simultaneously at t = 11 milliseconds. The difference between the front-end and door-end wall lateral displacements resulted from the added stiffness contributions from the aluminum extrusions found in the door-end wall. The maximum relative rotation within the road-side, wall-to-roof joint was 8°, occurring at approximately 15 milliseconds. This time corresponded to the time of peak lateral deflection of the roof panel.
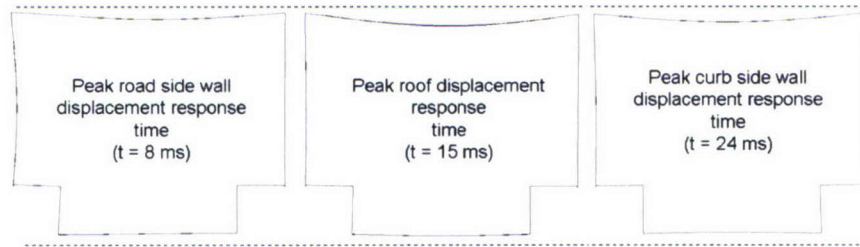

Figure 43. Deformations of Shelter Cross Section Through Central Blast Stiffener Plane at Various Response Times

Stress results for the road-side wall as the incident blast face were summarized and tabulated in table 7 in accordance with the local material axes described in figure 44 and the nodal location map shown in figure 45. Positive principal stresses represent the maximum principal stresses (σ_{p1}); negative principal stresses represent the minimum principal stresses (σ_{p2}); and $\sigma_{xy/max}$ is the maximum shear stress as computed in accordance with equations (22) and (23). The bolded stresses in table 7 require further mesh refinements and possibly localized models employing continuum elements to more accurately predict stresses in these regions.

*Table 7. Stress Results Summary for the Road-Side Wall as Incident Blast Face*

	Road Side Wall As Incident Blast Face (P_{so} = 2.5 psi)											
	Inner Face Sheet Stresses (psi)					Outer Face Sheet Stresses (psi)					Core Stresses (psi)	
Panel	σ_{xx}	σ_{yy}	$|\sigma_{xy}|^*$	σ_p	$|\sigma_{xy}|_{max}$	σ_{xx}	σ_{yy}	$|\sigma_{xy}|^*$	σ_p	$|\sigma_{xy}|_{max}$	σ_{zx}	σ_{zy}
Road Side Wall	23,110	40,660	1,402	40,771	14,937	-25,830	-43,790	384	-43,798	17,329	76	**144**
Roof	35,720	47,940	350	47,950	24,482	-38,410	-49,420	130	-49,422	22,531	**131**	**261**
Door End Wall	27,890	32,710	713	32,813	23,573	-42,470	-41,370	790	-42,883	16,661	103	**142**
Front Wall	24,740	33,640	367	33,655	15,039	-25,550	-35,010	1,073	-35,130	15,582	112	**137**
Curb Side Wall	12,660	24,180	801	24,235	8,833	-12,996	-26,257	700	-26,294	9,876	61	**137**
Floor & Wheel Wells	**-47,630**	**-93,330**	**27,002**	**-105,853**	27,023	**52,700**	**84,310**	**30,685**	**103,021**	30,685	**382**	**1,405**
All stresses reported in local material coordinate systems.												
* - Represents in-plane shear stress at max/min principal stress location.												
Bold values represent localized stress results that are not resolvable with global shelter model.												
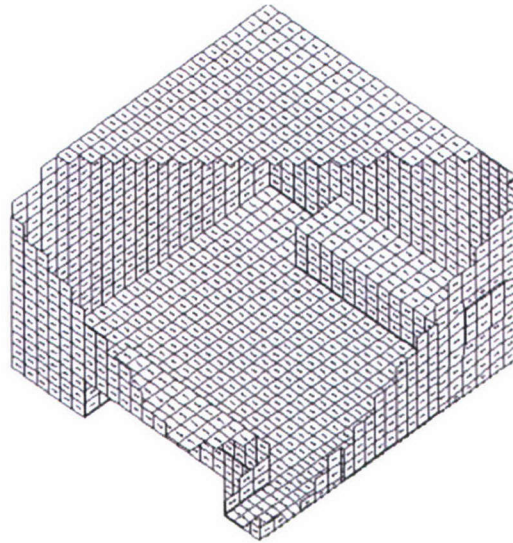
(The local Y-axis is orthogonal to the local X-axis
and lies in the element plane.)

***Figure 44. Local Material X-Direction Designated by Arrows for
Stress Output of Sandwich Elements***
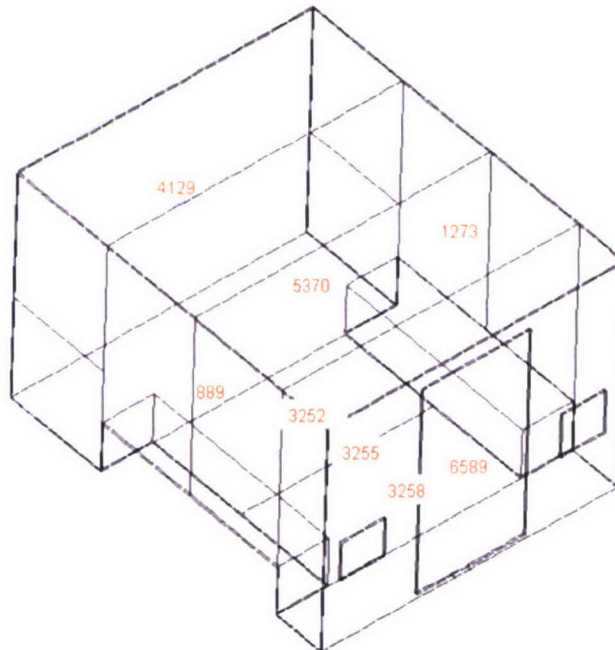
Node#	Location
889	Center of Road Side Wall
1273	Center of Curb Side Wall
3252	Floor Forward of Center Hoop Extrusion
3255	Floor at Center of Central Hoop Extrusion
3258	Floor Aft of Center Hoop Extrusion
4129	Center of Front End Wall
5370	Center of Roof
6589	Center of Door End Wall

Figure 45. Nodal Locations for Time-History Output

$$\sigma_{p1,p2} = \frac{\sigma_{xx} + \sigma_{yy}}{2} \pm \sqrt{\left(\frac{\sigma_{xx} - \sigma_{yy}}{2}\right)^2 + \sigma_{xy}^2} \,. \tag{22}$$

$$\sigma_{xy|max} = \pm\sqrt{\left(\frac{\sigma_{xx} - \sigma_{yy}}{2}\right)^2 + \sigma_{xy}^2} \,. \tag{23}$$

Contour plots of face sheet normal stresses σ_{xx} and σ_{yy} and honeycomb core transverse shear stresses σ_{zx} and σ_{zy} were plotted for individual panels and are shown in figures 46 through 93. Individual panel contour plots were necessary because, for dynamic events, the peak responses for all panels were not coincidental in time.

For the inner face sheet of the road-side wall, peak normal stresses σ_{xx} (figure 46) and σ_{yy} (figure 47) were 23,110 psi and 40,660 psi, respectively, and both occurred at the center at $t = 8$ milliseconds. At this time and center location (node 889), the magnitude of the in-plane shear stress σ_{xy} was 1402 psi. The corresponding maximum principal stress σ_{p1} for the inner face sheet was 40,771 psi at the center location (node 889), which exceeded the face sheet yield stress by 2%. The maximum in-plane shear stress σ_{xy} for the inner face sheet of the road-side wall was 14,937 psi (figure 48), which occurred near the forward lower corner. Normal stresses along the edges of the road-side-wall inner face sheet exhibited moderate compression that was indicative of limited rotational resistance provided by the D-extrusion joints. The maximum compressive σ_{xx} stress in the road-side-wall inner face sheet was −12,590 psi (figure 46), occurring adjacent to the upper end of the central blast stiffener. Likewise, the maximum compressive σ_{yy} stress in this inner face sheet was −31,200 psi (figure 47) at the same location.

For the outer face sheet, the maximum normal stresses σ_{xx} (figure 49) and σ_{yy} (figure 50) were −25,830 psi and -43,790 psi, respectively, occurring at the center. The magnitude of the in-plane shear stress σ_{xy} at the center of the outer face sheet was only 384 psi. The minimum principal stress σ_{p2} at the center of the outer face sheet was −25,822 psi, which was substantially below the face sheet yield stress. The maximum magnitude of the in-plane shear stress σ_{xy} for the outer face sheet was −17,329 psi (figure 51), which was localized along the rear vertical edge connecting the road-side wall and wheel-well assembly.

Transverse shear stresses σ_{zx} (figure 52) and σ_{zy} (figure 53) in the road-side-wall honeycomb core were 75.66 psi and 143.6 psi, respectively, which occurred along the edges.

For the road-side-wall as the incident blast face and $p_{so} = 2.5$ psi, stresses within the road-side wall face sheets and honeycomb core reached their allowable strength values. If yielding occurred in the actual structure, stresses in the face sheets would locally redistribute around the plastic region because of the limited amount of strain hardening (ductility) available; however, permanent deformation of the face sheets would result.
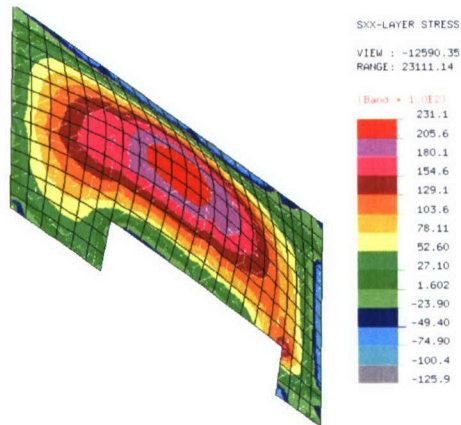
Figure 46. Contour Plot of σ_{xx} Stress for the Road-Side Wall Inner Face Sheet at Peak Response Time (t = 8 ms)
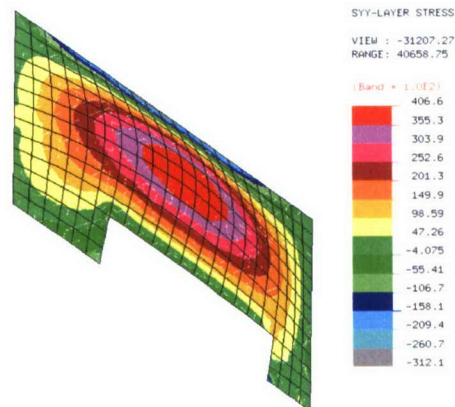

Figure 47. Contour Plot of σ_{yy} Stress for the Road-Side Wall Inner Face Sheet at Peak Response Time (t = 8 ms)
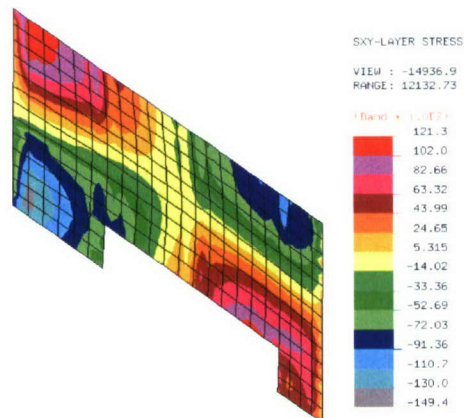

Figure 48. Contour Plot of σ_{xy} Stress for the Road-Side Wall Inner Face Sheet at Peak Response Time (t = 8 ms)
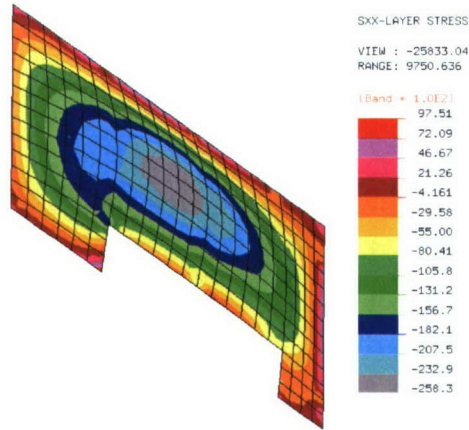
Figure 49. Contour Plot of σ_{xx} Stress for the Road-Side Wall Outer Face Sheet at Peak Response Time (t = 8 ms)
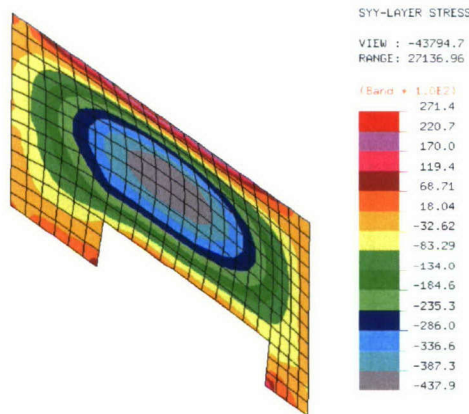

Figure 50. Contour Plot of σ_{yy} Stress for the Road-Side Wall Outer Face Sheet at Peak Response Time (t = 8 ms)

Figure 51. Contour Plot of σ_{xy} Stress for the Road-Side Wall Outer Face Sheet at Peak Response Time (t = 8 ms)

***Figure 52. Contour Plot of Honeycomb Core Transverse Shear Stress σ_{zx}
for the Road-Side Wall at Peak Response Time (t = 8 ms)***

***Figure 53. Contour Plot of Honeycomb Core Transverse Shear Stress σ_{zy}
for the Road-Side Wall at Peak Response Time (t = 8 ms)***

***Figure 54. Contour Plot of σ_{xx} Stress for the Roof Inner Face Sheet
at Peak Response Time (t = 15 ms)***

SYY-LAYER STRESS

VIEW : -29931.62
RANGE: 47943.24

(Band * 1.0E2)
479.4
423.8
368.2
312.6
256.9
201.3
145.7
90.06
34.43
-21.19
-76.82
-132.4
-188.1
-243.7
-299.3

Figure 55. Contour Plot of σ_{yy} Stress for the Roof Inner Face Sheet at Peak Response Time (t = 15 ms)

SXY-LAYER STRESS

VIEW : -19706.62
RANGE: 24482.18

(Band * 1.0E2)
244.8
213.3
181.7
150.1
118.6
87.00
55.44
23.88
-7.686
-39.25
-70.81
-102.4
-133.9
-165.5
-197.1

Figure 56. Contour Plot of σ_{xy} Stress for the Roof Inner Face Sheet at Peak Response Time (t = 15 ms)

SXX-LAYER STRESS

VIEW : -38407.36
RANGE: 25292.68

(Band * 1.0E2)
252.9
207.4
161.9
116.4
70.93
25.43
-20.07
-65.57
-111.1
-156.6
-202.1
-247.6
-293.1
-338.6
-384.1

Figure 57. Contour Plot of σ_{xx} Stress for the Roof Outer Face Sheet at Peak Response Time (t = 15 ms)

***Figure 58. Contour Plot of σ_{yy} Stress for the Roof Outer Face Sheet
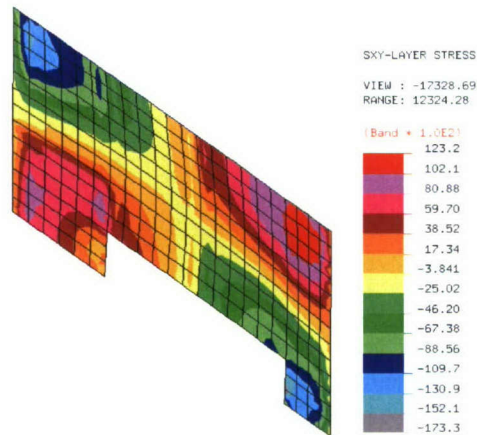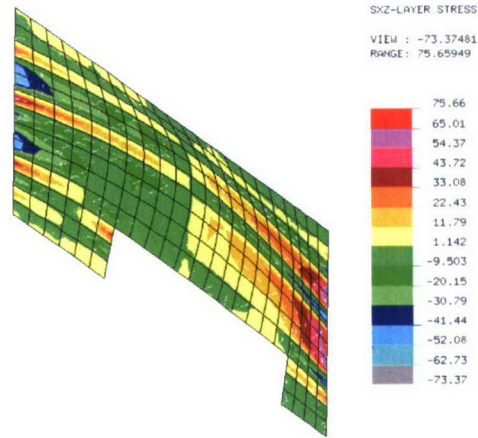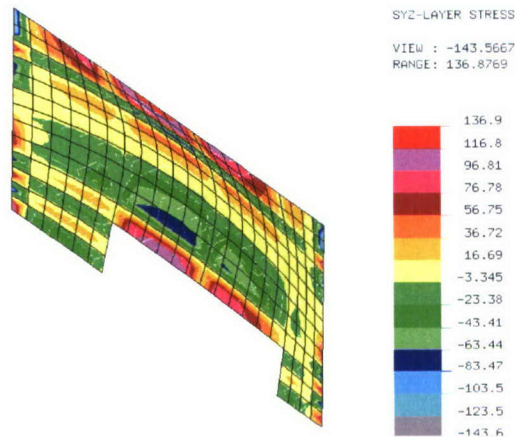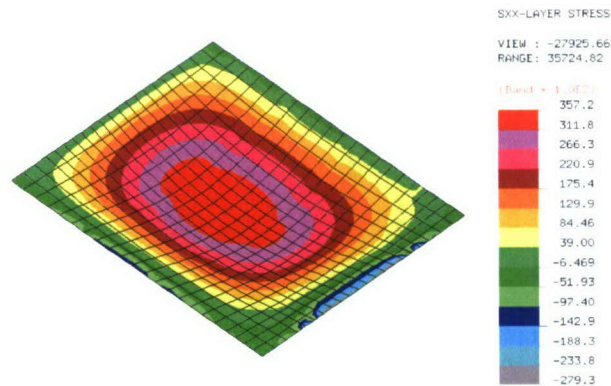at Peak Response Time (t = 15 ms)***

***Figure 59. Contour Plot of σ_{xy} Stress for the Roof Outer Face Sheet
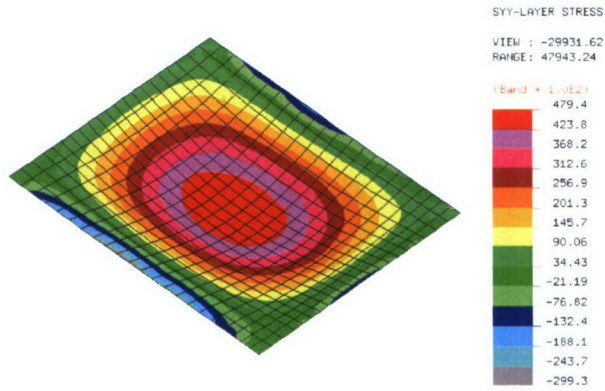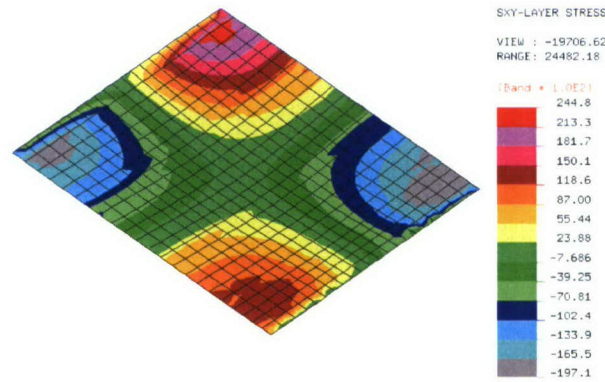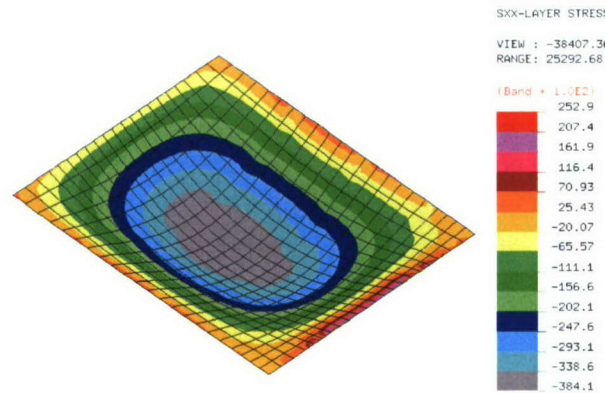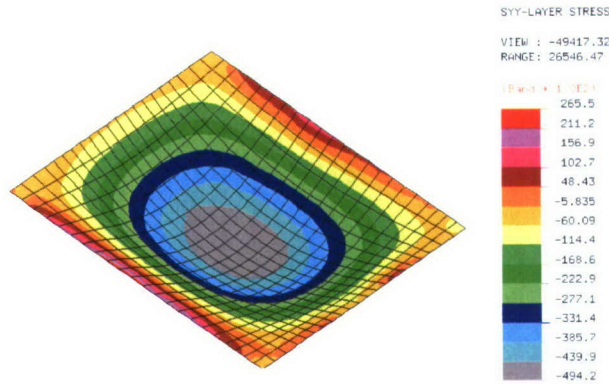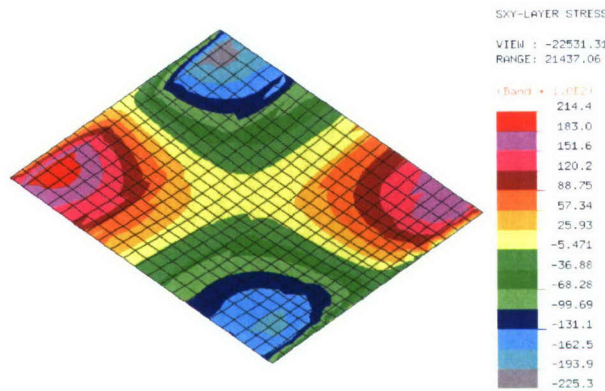at Peak Response Time (t = 15 ms)***

***Figure 60. Contour Plot of Honeycomb Core Transverse Shear Stress σ_{zx}
for the Roof at Peak Response Time (t = 15 ms)***

SYZ-LAYER STRESS

VIEW : -261.0952
RANGE: 217.8387

217.8
183.6
149.4
115.2
81.00
46.79
12.58
-21.63
-55.84
-90.05
-124.3
-158.5
-192.7
-226.9
-261.1
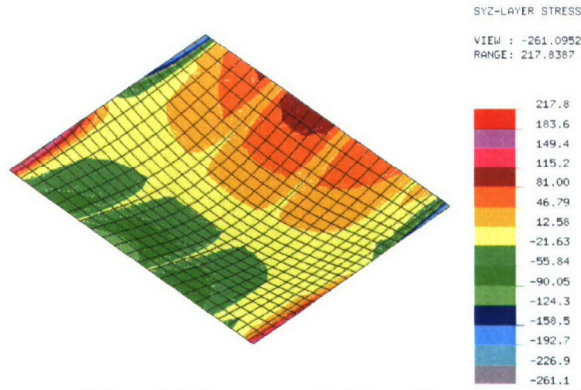
Figure 61. Contour Plot of Honeycomb Core Transverse Shear Stress σ_{zy} for the Roof at Peak Response Time (t = 15 ms)

SXX-LAYER STRESS

VIEW : -22459.93
RANGE: 27886.94

(Band * 1.0E2)
278.9
242.9
206.9
171.0
135.0
99.06
63.10
27.14
-8.827
-44.79
-80.75
-116.7
-152.7
-188.6
-224.6

Figure 62. Contour Plot of σ_{xx} Stress for the Door-End Wall Inner Face Sheet at Peak Response Time (t = 11 ms)

SYY-LAYER STRESS

VIEW : -47452.85
RANGE: 32706.5

(Band * 1.0E2)
327.1
269.8
212.6
155.3
98.04
40.78
-16.48
-73.73
-131.0
-188.2
-245.5
-302.8
-360.0
-417.3
-474.5

Figure 63. Contour Plot of σ_{yy} Stress for the Door-End Wall Inner Face Sheet at Peak Response Time (t = 11 ms)

47
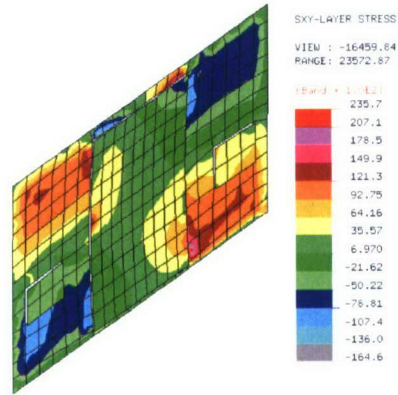
Figure 64. Contour Plot of σ_{xy} Stress for the Door-End Wall Inner Face Sheet at Peak Response Time (t = 11 ms)
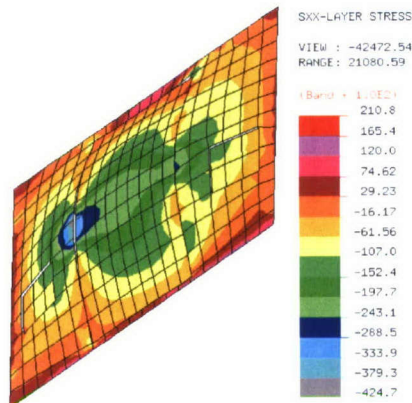
Figure 65. Contour Plot of σ_{xx} Stress for the Door-End Wall Outer Face Sheet at Peak Response Time (t = 11 ms)
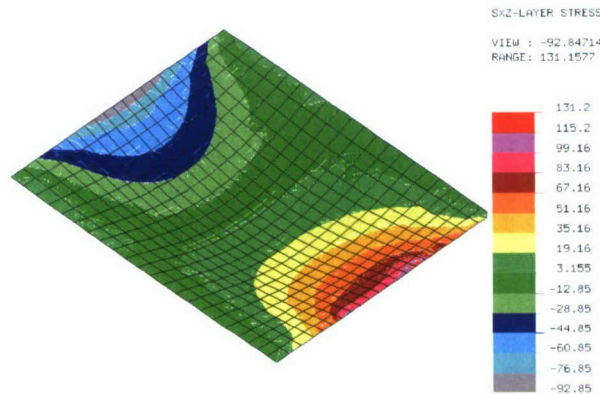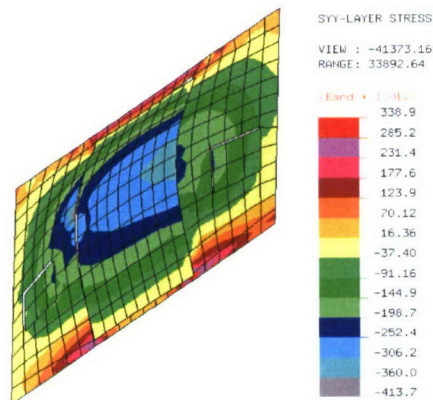

Figure 66. Contour Plot of σ_{yy} Stress for the Door-End Wall Outer Face Sheet at Peak Response Time (t = 11 ms)

48
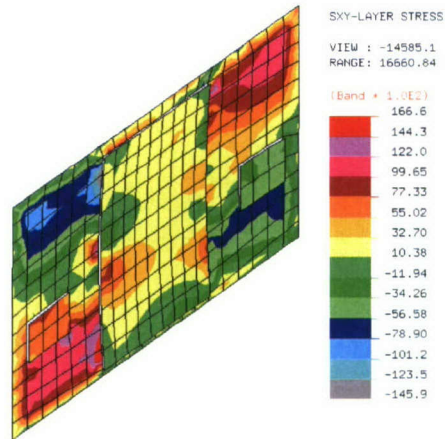
Figure 67. Contour Plot of σ_{xy} Stress for the Door-End Wall Outer Face Sheet at Peak Response Time (t = 11 ms)
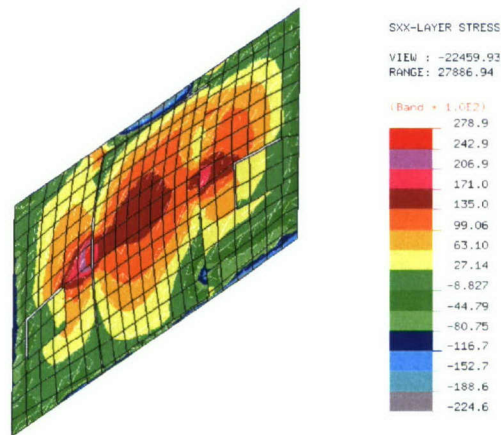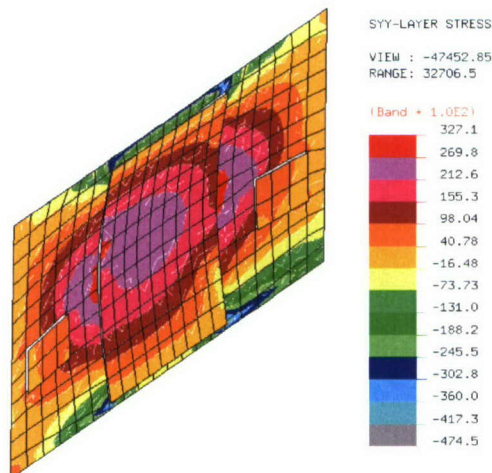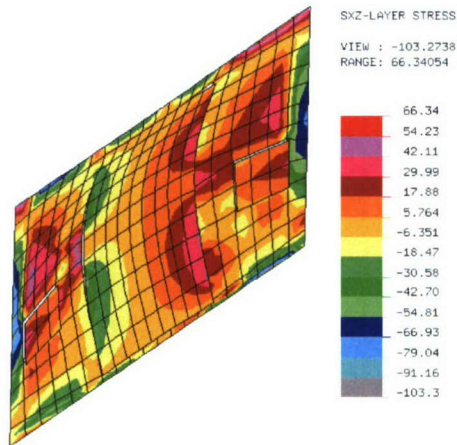

Figure 68. Contour Plot of Honeycomb Core Transverse Shear Stress σ_{zx} for the Door-End Wall at Peak Response Time (t = 11 ms)
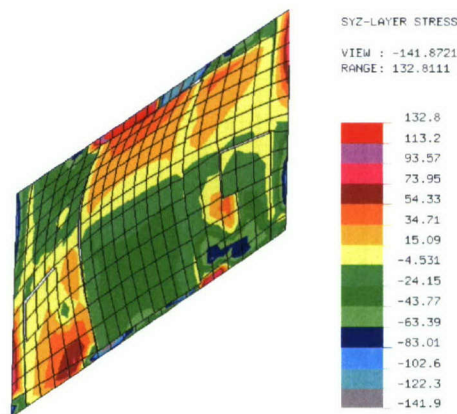
Figure 69. Contour Plot of Honeycomb Core Transverse Shear Stress σ_{zy} for the Door-End Wall at Peak Response Time (t = 11 ms)
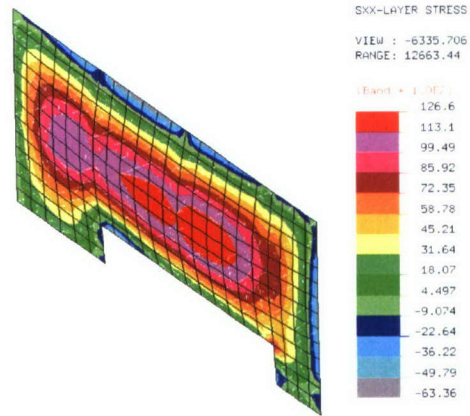
Figure 70. Contour Plot of σ_{xx} ***Stress for the Curb-Side Wall Inner Face Sheet
at Peak Response Time (t = 24 ms)***

Figure 71. Contour Plot of σ_{yy} ***Stress for the Curb-Side Wall Inner Face Sheet
at Peak Response Time (t = 24 ms)***

Figure 72. Contour Plot of σ_{xy} ***Stress for the Curb-Side Wall Inner Face Sheet
at Peak Response Time (t = 24 ms)***

Figure 73. Contour Plot of σ_{xx} Stress for the Curb-Side Wall Outer Face Sheet at Peak Response Time (t = 24 ms)

Figure 74. Contour Plot of σ_{yy} Stress for the Curb-Side Wall Outer Face Sheet at Peak Response Time (t = 24 ms)

Figure 75. Contour Plot of σ_{xy} Stress for the Curb-Side Wall Outer Face Sheet at Peak Response Time (t = 24 ms)

SXZ-LAYER STRESS

VIEW : -48.77746
RANGE: 60.69569

60.70
52.88
45.06
37.24
29.42
21.60
13.78
5.959
-1.860
-9.680
-17.50
-25.32
-33.14
-40.96
-48.78

Figure 76. Contour Plot of Honeycomb Core Transverse Shear Stress σ_{zx}
for the Curb-Side Wall at Peak Response Time (t = 24 ms)

SYZ-LAYER STRESS

VIEW : -98.39649
RANGE: 137.4212

137.4
120.6
103.7
86.89
70.04
53.20
36.36
19.51
2.668
-14.18
-31.02
-47.86
-64.71
-81.55
-98.40

Figure 77. Contour Plot of Honeycomb Core Transverse Shear Stress σ_{zy}
for the Curb-Side Wall at Peak Response Time (t = 24 ms)

SXX-LAYER STRESS

VIEW : -21117.15
RANGE: 24744.88

(Band * 1.0E2)
247.4
214.7
181.9
149.2
116.4
83.66
50.90
18.14
-14.62
-47.38
-80.14
-112.9
-145.7
-178.4
-211.2
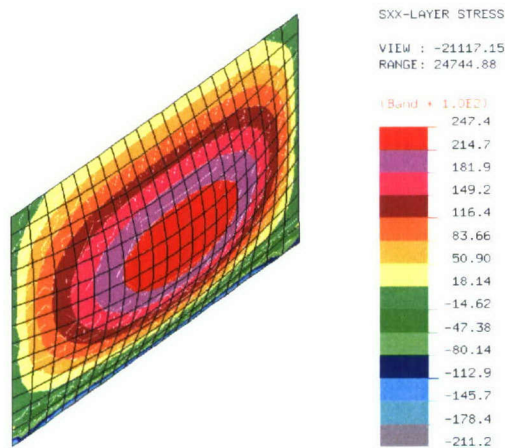
Figure 78. Contour Plot of σ_{xx} Stress for the Front-End Wall Inner Face Sheet
at Peak Response Time (t = 31 ms)
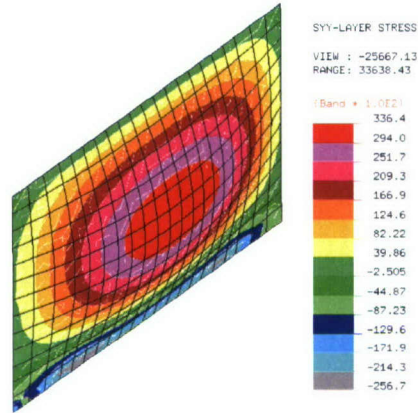
Figure 79. Contour Plot of σ_{yy} Stress for the Front-End Wall Inner Face Sheet at Peak Response Time (t = 31 ms)
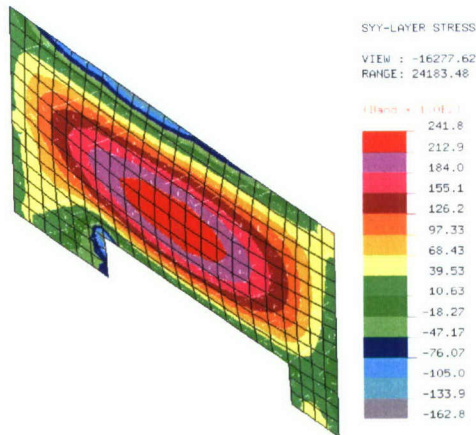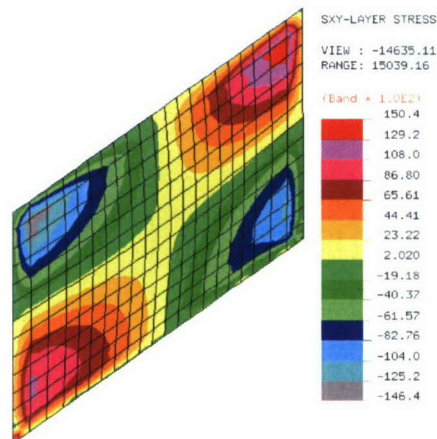

Figure 80. Contour Plot of σ_{xy} Stress for the Front-End Wall Inner Face Sheet at Peak Response Time (t = 31 ms)
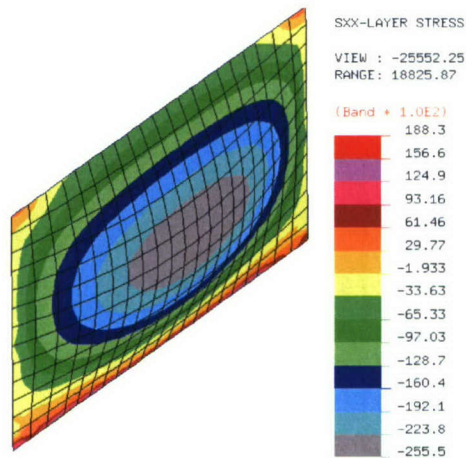
Figure 81. Contour Plot of σ_{xx} Stress for the Front-End Wall Outer Face Sheet at Peak Response Time (t = 31 ms)
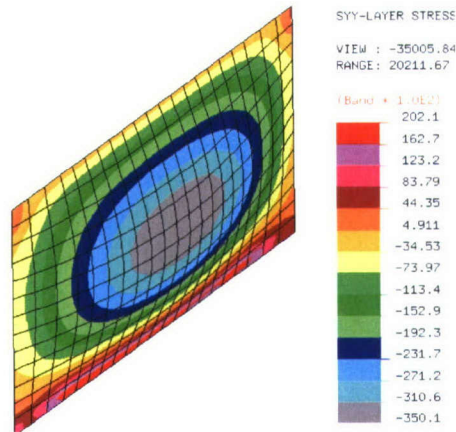
***Figure 82. Contour Plot of σ_{yy} Stress for the Front-End Wall Outer Face Sheet
at Peak Response Time (t = 31 ms)***
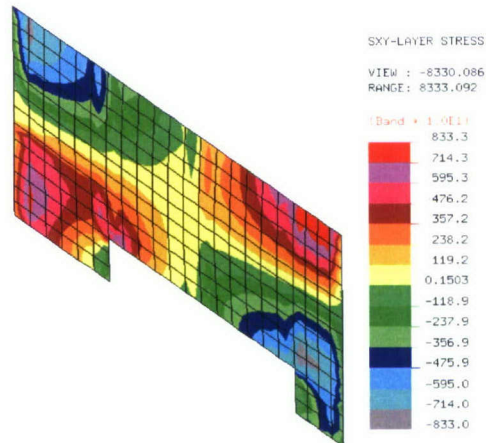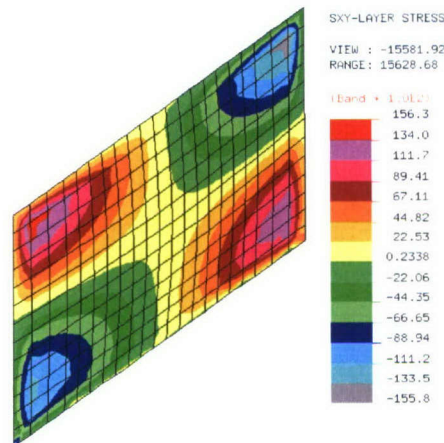

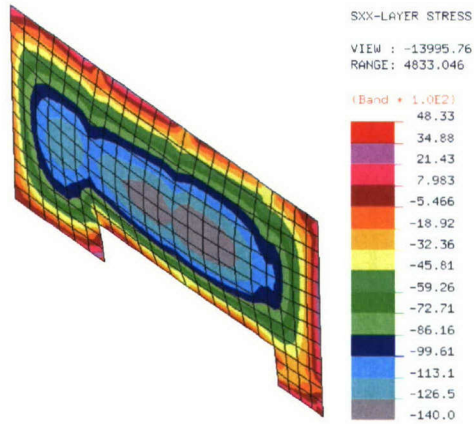***Figure 83. Contour Plot of σ_{xy} Stress for the Front-End Wall Outer Face Sheet
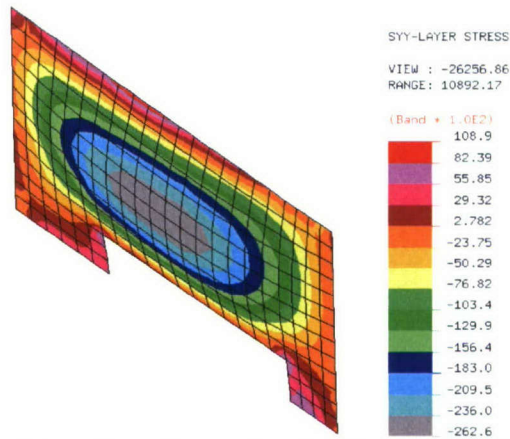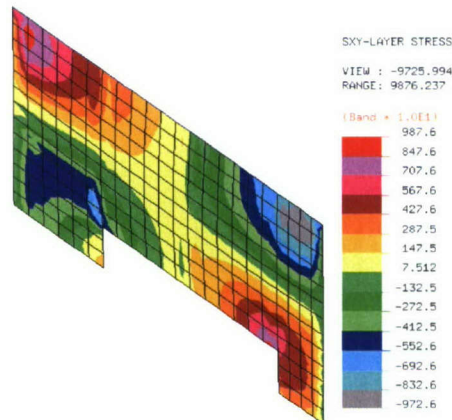at Peak Response Time (t = 31 ms)***
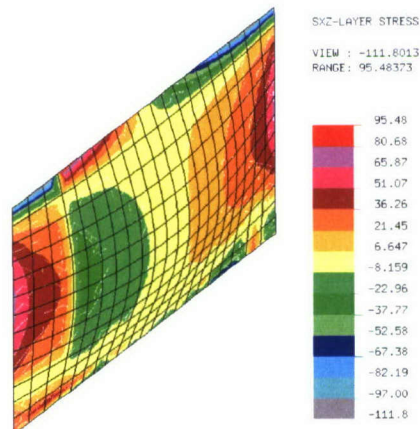
***Figure 84. Contour Plot of Honeycomb Core Transverse Shear Stress σ_{zx}
for the Front-End Wall at Peak Response Time (t = 31 ms)***

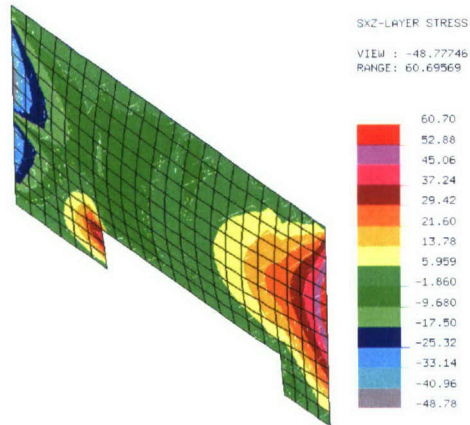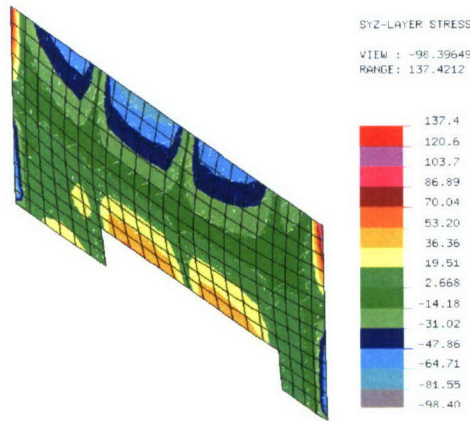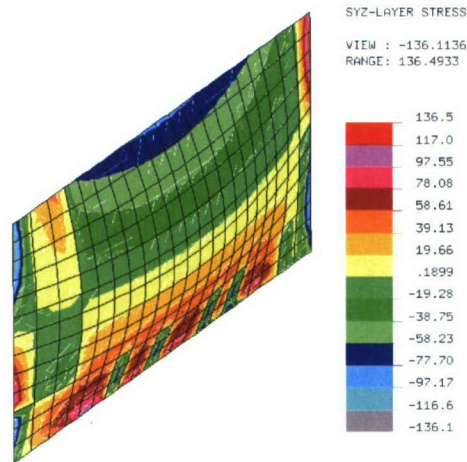*Figure 85. Contour Plot of Honeycomb Core Transverse Shear Stress σ_{zy} for the Front-End Wall at Peak Response Time (t = 31 ms)*
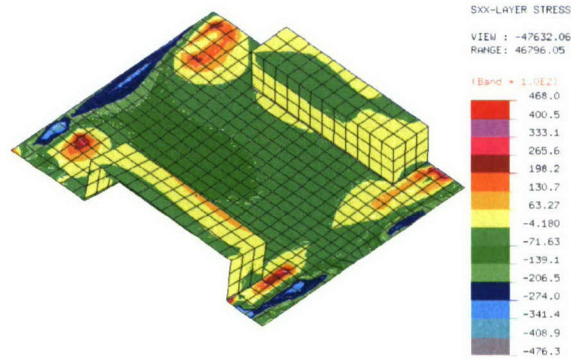
Figure 86. Contour Plot of σ_{xx} Stress for the Floor and Wheel-Well Inner Face Sheet at Peak Response Time (t = 12 ms)
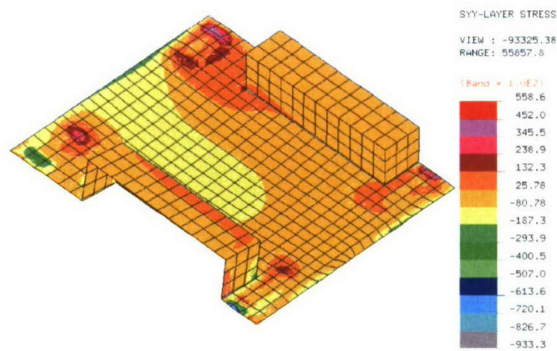
Figure 87. Contour Plot of σ_{yy} Stress for the Floor and Wheel-Well Inner Face Sheet at Peak Response Time (t = 12 ms)

Figure 88. Contour Plot of σ_{xy} Stress for the Floor and Wheel-Well Inner Face Sheet at Peak Response Time (t = 12 ms)
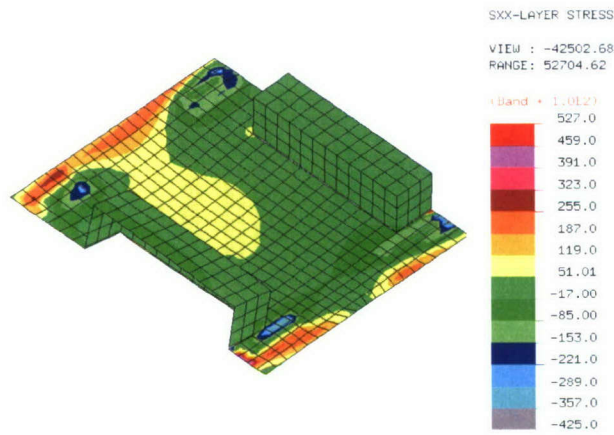
Figure 89. Contour Plot of σ_{xx} Stress for the Floor and Wheel-Well Outer Face Sheet at Peak Response Time (t = 12 ms)
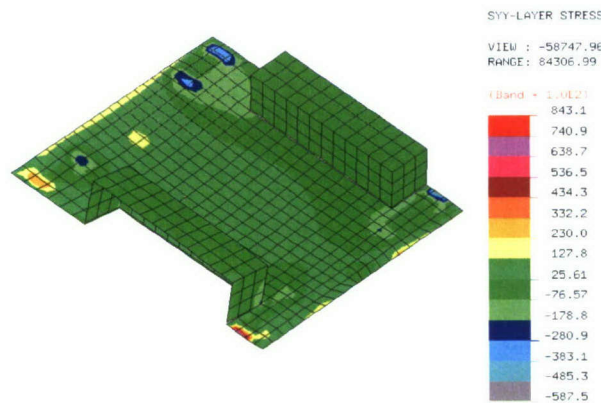
Figure 90. Contour Plot of σ_{yy} Stress for the Floor and Wheel-Well Outer Face Sheet at Peak Response Time (t = 12 ms)

Figure 91. Contour Plot of σ_{xy} Stress for the Floor and Wheel-Well Inner Face Sheet at Peak Response Time (t = 12 ms)
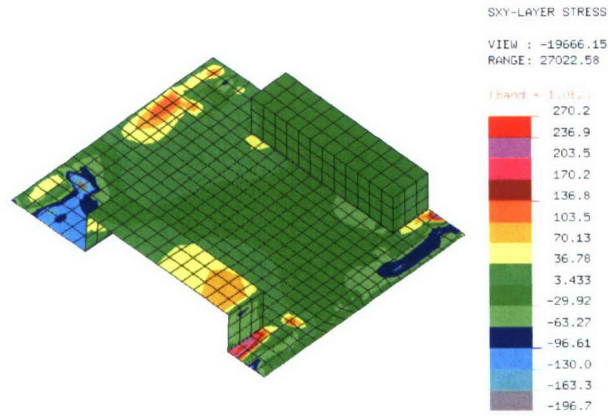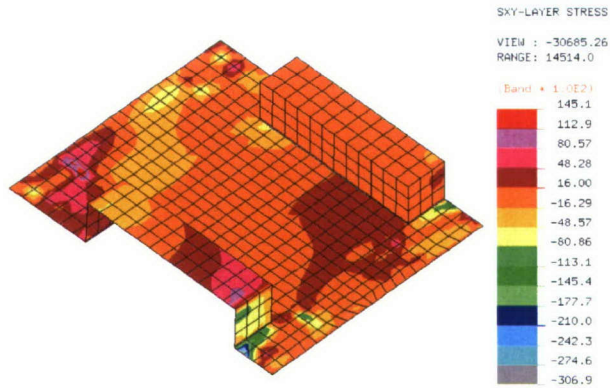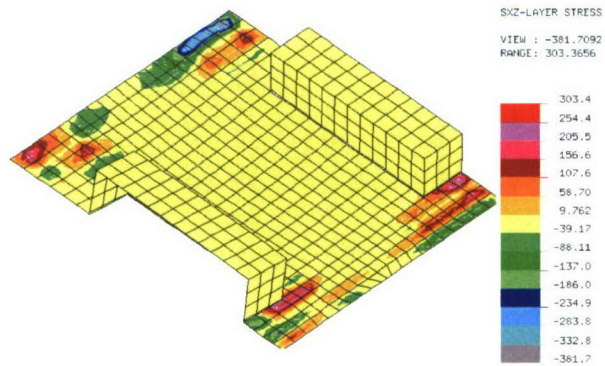

Figure 92. Contour Plot of Honeycomb Core Transverse Shear Stress σ_{zx} for the Floor and Wheel Well at Peak Response Time (t = 12 ms)
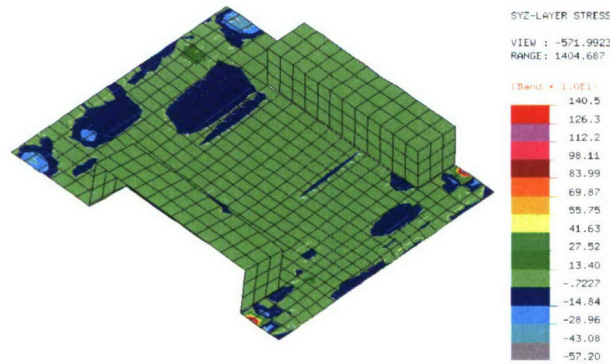

Figure 93. Contour Plot of Honeycomb Core Transverse Shear Stress σ_{zy} for the Floor and Wheel Well at Peak Response Time (t = 12 ms)

57

Peak normal stresses in the roof inner face sheet occurred at the center (node 5370) as shown in figures 54 and 55, with σ_{xx} = 35,720 psi and σ_{yy} = 47,940 psi at t = 15 milliseconds. At the roof center, the magnitude of the in-plane shear stress σ_{xy} (figure 56) for this face sheet was 350 psi. The corresponding maximum principal stress σ_{p1} at this location was 47,950 psi, which exceeded yield by 20%. Because this principal stress exceeded the face sheet yield stress by 20%, the roof would expectedly deform in a plastic manner; however, this inner face sheet principal stress was within 2.0% of the ultimate stress. A nonlinear plasticity model is recommended to investigate the effects of yielding on the redistribution of stress in the roof face sheets and to ensure sufficient ductility to prevent fracture. As with the road-side wall, stresses along the edges of the roof inner face sheet exhibited moderate compression, suggesting that some rotational resistance was provided from the D-extrusion joints. The maximum magnitude of in-plane shear stress σ_{xy} for the roof inner face sheet was 24,482 psi, occurring adjacent to the front wall/curb-side wall corner.

For the outer face sheet, the maximum compressive values of normal stresses σ_{xx} (figure 57) and σ_{yy} (figure 58) at the center location were –38,410 and –49,420 psi, respectively. The corresponding magnitude of in-plane shear stress σ_{xy} for the outer face sheet was 130 psi. The resulting minimum principal stress σ_{p2} was –38,408 psi and was slightly below the compressive yield stress. The maximum magnitude of in-plane shear stress σ_{xy} for the outer face sheet of the roof was 22,531 psi (figure 59) at the same location for that of the inner face sheet.

Contour plots of the in-plane shear stress σ_{xy} in both roof face sheets exhibited nearly antisymmetric patterns as expected. Distributions of honeycomb core transverse shear stresses in the roof were also nearly antisymmetric as shown in figures 60 and 61. The presence of the blast extrusions in the roof had a noticeable effect on the distribution of honeycomb core transverse shear stress σ_{zy}. Peak values of the honeycomb core transverse shear stresses σ_{zx} (figure 60) and σ_{zy} (figure 61) were 131.2 psi and 261.1 psi, respectively, occurring along the front and rear edges at t = 15 milliseconds. These peak shear stresses, which were considered highly localized, could not, however, be resolved with the global shelter model. Substructural models of the roof edge regions using solid (continuum) elements of the face sheets, honeycomb core, extrusions, and fasteners would be required. Away from the localized peaks, the honeycomb core transverse shear stresses were within the allowable strength.

The solution time of interest was based on capturing peak stresses and displacements of the various shelter panels. During this time, the door-end wall was subjected to a time-varying positive overpressure, whereby the door remained in continuous contact with the frame surrounding the door opening. The X-displacement time-history plot (see figure 42) shows there were no instances of outward (+X) displacements of the door panel. Therefore, two load transfer paths existed for the door, namely through the hinges/latch mechanisms and by contact with the frame of the door opening. Rigid link elements were used to kinematically couple the displacements between the door and the door opening frame to simulate the contact effects. If the door panel had oscillated between inward and outward displacement modes, a geometrically nonlinear model would be required. Upon any outward door panel motions resulting from either dynamic rebound or negative pressure loading, the hinges and latch mechanisms would have transferred the total door load to the door-end wall. For such a case, the hinges and latching mechanisms would require meshing in a substructural model of both the door and door-end wall.

The peak inner face sheet normal stresses σ_{xx} and σ_{yy} of the door-end wall were 27,890 psi and 32,710 psi, respectively, both occurring locally near the central hinge at $t = 11$ milliseconds. The magnitude of the corresponding in-plane shear stress σ_{xy} for this location was only 713 psi. The maximum principal stress σ_{p1} for the inner face sheet near the central hinge was 32,813 psi and was below yield. The maximum magnitude for the in-plane shear stress σ_{xy} for the inner face sheet was 23,573 psi, which occurred along the curb-side, vertical edge of the door opening.

For the outer face sheet, the peak compressive normal stresses σ_{xx} and σ_{yy} for the door-end wall were −42,470 psi and −41,370 psi, respectively, with both occurring near the central hinge. At this location, the magnitude of the corresponding in-plane shear stress σ_{xy} was 1073 psi, resulting in a −40,957-psi minimum principal stress σ_{p2}, which slightly exceeded yield by 2%, for the door-end wall outer face sheet that. The maximum magnitude of in-plane shear stress σ_{xy} for the outer face sheet was 16,661 psi, which occurred along the road-side vertical edge of the door opening. Along the edges of the door-end wall, regions of stress reversal due to the rotational joint stiffnesses were observed. It was noted that the delayed pressure on the curb-side wall resulted in an unbalanced loading effect that led to racking deformations in both end walls. These deformations significantly increased the magnitudes of in-plane shear stress exerted on the end-wall face sheets. Peak values of honeycomb transverse shear stresses σ_{zx} and σ_{zy} were 101.6 psi and 145.8 psi, respectively. These peak values were highly localized along the bottom edge of the door-end wall.

The peak response time of the front-end wall matched that of the door end wall, namely $t = 11$ milliseconds, as both were subjected to only the overpressure. Peak normal stresses σ_{xx} and σ_{yy} of the inner face sheet were 24,740 psi and 33,640 psi, respectively, with both occurring at the center (node 4129). At this location, the magnitude of in-plane shear stress σ_{xy} was 367 psi. The maximum magnitude of the in-plane shear stress σ_{xy} for the inner face sheet was 15,039 psi, which occurred at the upper corner near the road-side wall. The maximum principal stress σ_{p1} at the center of the inner face sheet was 33,655 psi and was below yield. For the outer face sheet, the maximum compressive normal stresses σ_{xx} and σ_{yy} were −25,550 psi and −35,010 psi, respectively, occurring at the center. The magnitude of the in-plane shear stress σ_{xy} at this location was 1,073 psi. The maximum magnitude of the in-plane shear stress σ_{xy} for the outer face sheet of the front-end wall was 15,582 psi, occurring at the upper corner near the road-side wall. Stress reversals were observed along each edge of the front wall face sheets and were indicative of rotational resistance afforded by the D-extrusion joints. These reversals, however, were more dominant along the lower edge of the front wall. The distributions of in-plane shear stresses for both face sheets were nearly antisymmetric. Peak values of the honeycomb transverse shear stresses σ_{zx} and σ_{zy} were 111.8 psi and 136.5 psi, respectively, and were highly localized along the edges.

Stresses in the curb-side wall reached their peak values at the arrival time, t_a, of 24 milliseconds. Maximum values of inner face sheet normal stresses σ_{xx} and σ_{yy} for the curb side wall were 12,660 psi and 24,180 psi, respectively, occurring at the center. At this location, the in-plane shear stress σ_{xy} was 801 psi. The subsequent maximum principal stress σ_{p1} at the center location was 24,235 psi. The maximum magnitude of in-plane shear stress σ_{xy} for the

inner face sheet was 8,833 psi, occurring near the forward upper corner. Distribution of the inner face sheet normal stresses indicated some limited rotational resistance of the D-extrusion joints as evidenced by stress reversals along the edges of the curb side wall. For the outer face sheet, the maximum compressive normal stresses σ_{xx} and σ_{yy} were –13,996 psi and –26,257 psi, respectively, occurring at the center. At this location, the magnitude of the corresponding in-plane shear stress σ_{xy} was approximately 700 psi. The resulting minimum principal stress σ_{p2} was –26,294 psi. The maximum magnitude of in-plane shear stress σ_{xy} for the outer face sheet was 9876 psi, which resided at the same location as that of the inner face sheet. The maximum values of honeycomb core transverse shear stresses σ_{zx} and σ_{zy} were 60.7 psi and 137.4 psi, respectively. Both occurred along the vertical edges of the curb-side wall, with the latter being highly localized. The variation of core shear stress σ_{zy} indicated that the blast hoop stiffeners locally reduced this stress within the honeycomb layer. Recall that the curb-side wall was subjected to the overpressure and that the road-side wall was subjected to the reflected and dynamic pressures; the normal stresses within the curb-side wall were noticeably less than those reported for the road-side wall.

Stress contour plots for the floor and wheel-well components were reported together in figures 86 through 93. Overall, the peak stresses were observed at the mounting-kit fastener locations. Remote from these peak locations, stresses for the face sheets and honeycomb core were within the prescribed allowable values. Maximum stress components and principal stresses were tabulated in table 7 for the face sheets and core of the floor and wheel well panels.

The extruded aluminum blast hoop stiffeners provided resistance to lateral deflections and, to a lesser degree, racking deformations. The differences in the pressures and arrival times between the road- and curb-side walls resulted in an unbalanced loading effect. This unbalance led to racking deformations in the door- and front-end walls. The blast hoop stiffeners acted as beams subjected to distributed loads with finite rotational stiffnesses at their ends. This was evidenced by the fact that the peak bending moments developed along the ends of each stiffener segment. The corresponding maximum bending stresses, σ_{xx}, for each blast stiffener were computed using the following generalized flexure stress equation (24) and are listed in table 8:

$$\sigma_{xx} = \frac{M_z y}{I_z} + \frac{M_y z}{I_y}, \qquad (24)$$

where M_z = moment about local z-axis,

M_y = moment about local y-axis,

y = section outer width/2,

z = section outer height/2,

I_y = area moment of inertia about local y-axis,

I_z = area moment of inertia about local z-axis.

60

Table 8. Maximum Bending Stresses in Blast Hoop Stiffeners for Road-Side Wall Blast

Road Side Wall As Incident Blast Face, Pso = 2.5 psi			
Hoop	Maximum Bending Stress (psi)	Element#	Location
Forward	21,193	3487	Road side wall end adjacent to roof.
Center	24,647	3149	Road side wall end adjacent to roof.
Rear	33,105	3652	Road side wall end adjacent to floor.

Since the beam elements used to discretize the blast hoop stiffeners consisted of two local nodes, namely node #1 and node #2, separate bending stress versus time history plots were required for each node. The time history curves of peak σ_{xx} values were separately plotted in figures 94 through 99 for each segment end of the three blast hoop stiffeners (forward, center, and rear). Figure 100 shows the element number locations referenced in the time history plot legends.

Figure 94. Time History Plot of Peak σ_{xx} Stress for the Forward Blast Hoop Stiffener at Beam Element Local #1 Nodes

Figure 95. Time History Plot of Peak σ_{xx} Stress for the Forward Blast Hoop Stiffener at Beam Element Local #2 Nodes

Figure 96. Time History Plot of Peak σ_{xx} Stress for the Center Blast Hoop Stiffener at Beam Element Local #1 Nodes

Figure 97. Time History Plot of Peak σ_{xx} Stress for the Center Blast Hoop Stiffener at Beam Element Local #2 Nodes
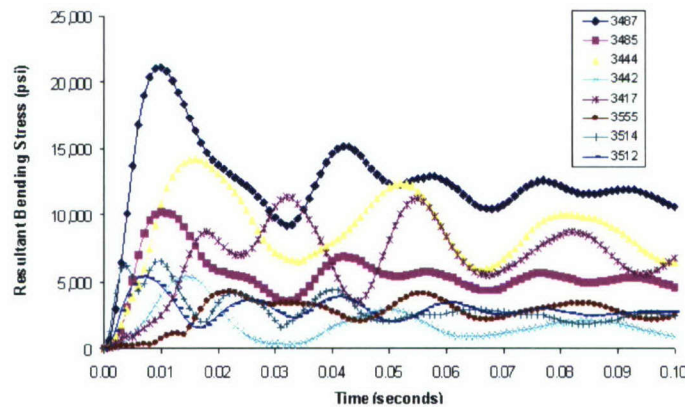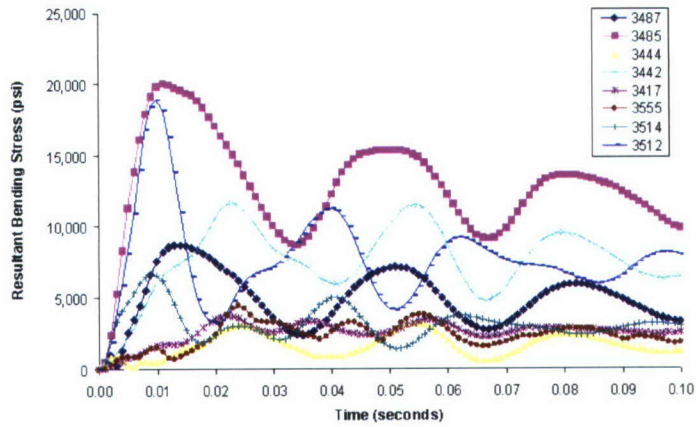
62

Figure 98. Time History Plot of Peak σ_{xx} Stress for the Rear Blast Hoop Stiffener at Beam Element Local #1 Nodes

Figure 99. Time History Plot of Peak σ_{xx} Stress for the Rear Blast Hoop Stiffener at Beam Element Local #2 Nodes
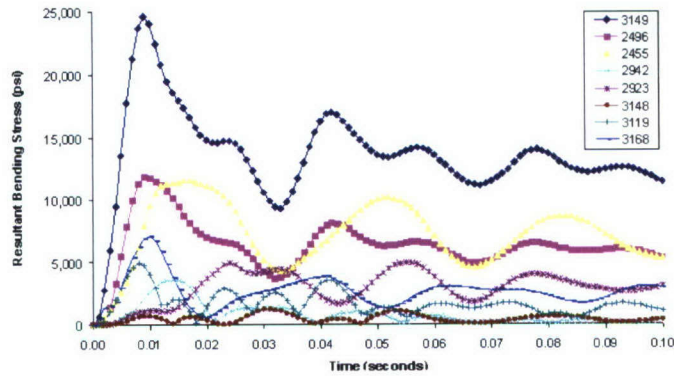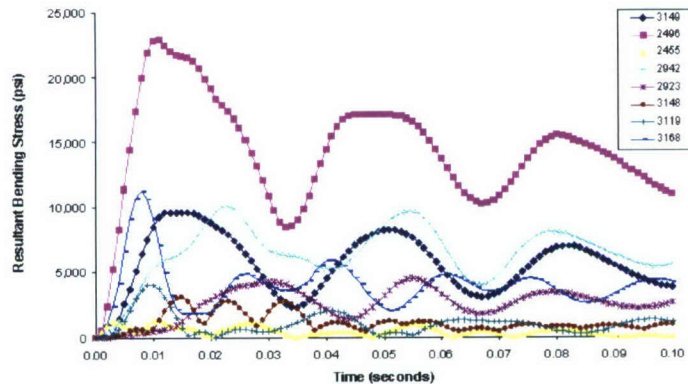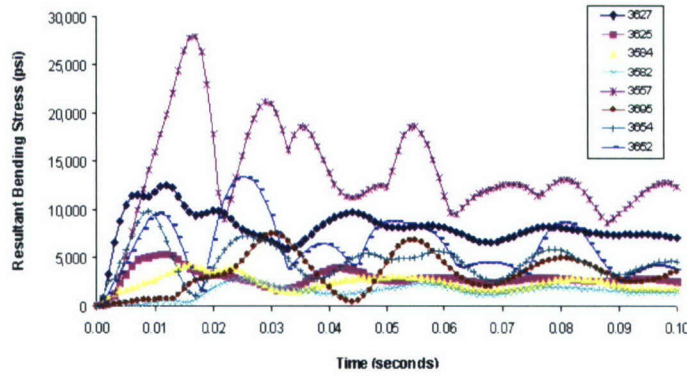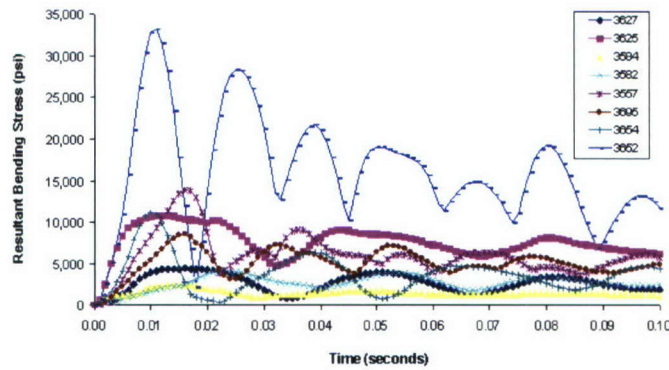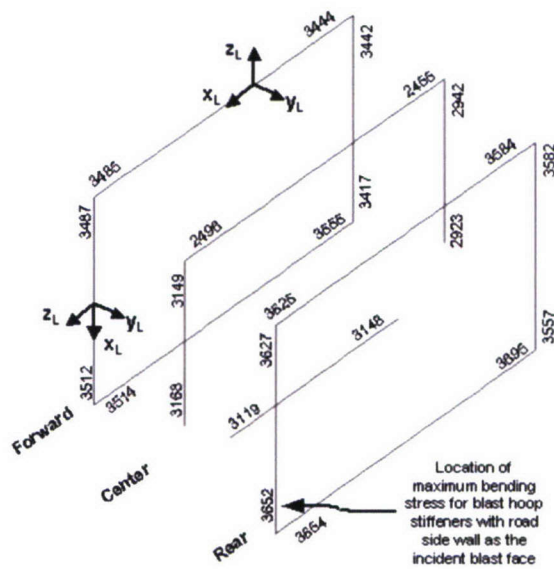

Figure 100. Blast Hoop Stiffener Beam Elements and Local Coordinate Systems

63

Overall, the predicted stresses for the 2.5-psi road-side wall blast case indicated that the nonintegrated (empty) shelter was stressed to, and, in some locations, slightly beyond the allowable material strengths and the limits of linear elasticity. The peak lateral deflections for each panel surface were considered commensurate with the shelter construction and dynamic loads. The maximum rotation between the road-side wall and roof joint was 8°, occurring at approximately 15 milliseconds. This time corresponded to the time of peak lateral deflection of the roof panel. Note that this 8°rotation was only 1° greater than the maximum rotation witnessed for the same joint in the static section tests—confirming that the D-extrusion joints provided limited rotational stiffness during the blast event. It is expected that any integration of electronic equipment racks inside the shelter could provide mounting configurations that, perhaps, may stiffen the shelter and reduce panel deflections.

As shown in table 7, principal stresses for the face sheets of the roof, side, and end walls were stressed from below yield to as high as 20% beyond yield. For those regions where principal stresses exceeded yield, some level of plastic deformation occurred. Peak stresses for the wheel-well and floor panels were highly localized at the mounting kit fastener regions and could not be resolved with the current global model. Substructural modeling is recommended to ascertain whether these values were analytical anomalies or realistic stresses. Bending stresses of the blast hoop stiffeners were predicted to be below their yield stress. Results of this blast case and those of the curb-side wall as the incident face were assumed to be identical because the shelter possesses nearly complete lateral symmetry (both geometrically and materially). The unsymmetrical arrangement of door hinges and latch mechanisms prevented the assumption of complete symmetry, but such features were considered to have inconsequential effects from a global response perspective.

The maximum bending stress among all the blast hoop stiffener elements was 33,105 psi, which occurred at 11 milliseconds along the road-side wall segment of the rear blast hoop stiffener at the end adjacent to the floor. This maximum stress location is explained as follows. In addition to the local M_y bending moments, primarily due to the reflected pressure exerted upon the road-side wall, the rear blast hoop stiffener supported a substantial M_z bending moment due to the overpressure loading exerted upon the door-end wall. Furthermore, because the rear blast hoop stiffener was located closer to the door-end wall than the forward blast hoop stiffener was located to the front-end wall, the rear stiffener was subjected to a greater combination of bending moments. Although the front and center blast hoop stiffeners were also subjected to M_z bending moments, there magnitudes were less. The factor of safety against yielding for the rear blast hoop stiffener was 1.21.

CONCLUSIONS

Sandwich panel construction, which is widely used in aircraft design, is particularly advantageous for meeting the stringent structural and weight requirements of mobile military systems. When properly designed for a prescribed flexural rigidity, SPC can provide an order of magnitude weight reduction over homogeneous panel construction.

This investigation demonstrated that using aluminum face sheet/paper honeycomb core SPC systems provides another advantage by decoupling the normal and transverse shearing stresses among the constituent materials when $E_c << E_f$. This decoupling enables the designer to individually tailor the bending and transverse shearing responses, allowing for additional weight reductions.

Sandwich panel construction, however, raises the level of engineering complexities required for proper design practices and avoidance methods for structural failure modes that are not an issue for homogeneous panel construction. For example, unlike, HPC, SPC must deal with interlaminar shear, face sheet/core delaminations, core crushing, etc. Furthermore, SPC requires using close-out extrusions to enable interconnectivity of adjacent panels. Here, the localized mechanical behavior at the panel/extrusion connections, which is often unknown and difficult to predict, can significantly influence the global response of the structure. As shown in this report, rotational stiffnesses at these interfaces were required and were subsequently determined through substructural testing and later incorporated as kinematic parameters in the full-shelter models.

The material level and substructural level tests were indispensable steps in ensuring continued accuracy of the sandwich element and proper representation of the local joint rotational stiffnesses. Both levels of testing were necessary in developing the full global shelter models for accurate predictions of mode shapes, frequencies, and dynamic air blast responses.

REFERENCES

1. *Metals Handbook Desk Edition*, American Society of Metals, 1985.

2. "Mechanical Properties of Hexcel Honeycomb Materials," Technical Service Bulletin 120, Hexcel Corporation, Stamford, CT, 1992.

3. J. R. Vinson, *The Behavior of Sandwich Structures of Isotropic and Composite Materials*, Technomic Publishing Co., Lancaster, PA, 1999.

4. H. G. Allen, *Analysis and Design of Structural Sandwich Panels*, Pergamon Press, Oxford, UK, 1969.

5. A. C. Ugural and S. K. Fenster, *Advanced Strength and Applied Elasticity*, Elsevier, Amsterdam, 1977.

6. S. Timoshenko, *Strength of Materials*, D. Van Nostrand Company, Inc., Princeton, NJ, 1953.

7. NISA, Version 11.0, Engineering Mechanics Research Corporation, Troy, MI.

8. K. J. Bathe, *Finite Element Procedures in Engineering Analysis*, Prentice-Hall, Englewood Cliffs, NJ, 1982.

9. J. Frantz, D. C. Kammer, M. Baker, and S. Pincura, "Shock and Vibration Analysis of a Communication Shelter Subject to Nuclear Blast," Military Communications (MILCOM) Conference, Monterey, CA, October 5-9, 1986.

10. C. M. Harris and C. E. Crede, *Shock & Vibration Handbook*, McGraw-Hill, New York, 1961.

INITIAL DISTRIBUTION LIST

Addressee	No. of Copies
U.S. Army Natick Soldier Research, Development, and Engineering Center, Natick, MA (J. Cullinane, J. Roche, T. Reynolds, F. Kostka, T. Godfrey, J. Miletti, R. Benny, G. Gildea, G. Thibault)	9
Army Research Laboratory, Langley (MS-188E (A. R. Johnson))	1
Army Research Laboratory, Aberdeen Proving Grounds, MD (AMSRD-ARL-WM-MD (R. Dooley, B. Cheeseman, D. Granville))	3
Army Research Laboratory, Adelphi, MD (AMSRL-SE-RE (Y. Lee))	1
U.S. Army Research Office (AMSRD-ARL-RO-EN (A. Rajendran))	1
Naval Surface Warfare Center, Carderock Division, W. Bethesda, MD (Code 65 (R. Crane, E. Rasmussen))	2
Office of Naval Research (ONR-331 (R. Barsoum), ONR-334 (Y. Rajapakse))	2
Defense Technical Information Center	2
Center for Naval Analyses	1
The City College of New York, New York, NY (A. Sadegh)	1